



# The effects of temperature and pressure on the physical properties and stabilities of point defects and defect complexes in B1-ZrC



Guanlin Yang<sup>a</sup>, Meiling Xiong<sup>a</sup>, Yulu Zhou<sup>a</sup>, Xiaoma Tao<sup>a</sup>, Qing Peng<sup>b,c</sup>, Yifang Ouyang<sup>a,\*</sup>

<sup>a</sup> Guangxi Key Laboratory of Processing for Non-ferrous Metallic and Featured Materials, School of Physical Science and Technology, Guangxi University, Nanning 530004, People's Republic of China

<sup>b</sup> Physics Department, King Fahd University of Petroleum & Minerals, Dhahran 31261, Saudi Arabia

<sup>c</sup> KACARE Energy Research & Innovation Center at Dhahran, Dhahran, 31261, Saudi Arabia

## ARTICLE INFO

### Keywords:

ZrC

Point defect

Gibbs energy

First-principles calculations

## ABSTRACT

With high stiffness, B1-ZrC in rocksalt structure is a hard structural material for various applications in harsh environments, whereas its tolerance of defects is elusive. Herein, we have investigated the stability and physical properties of B1-ZrC with point defects under high temperature and pressure by means of first-principles calculations accompanied with the quasi-harmonic Debye model. Our results illustrated that the introduction of point defects usually degrades the thermophysical properties. The formations of different point defects with the effects of temperature and pressure are characteristic and classifiable. The accumulation of point defects is in an orderly manner. Carbon vacancies and their complexes are the major point defects in population. The Gibbs energies of formation and concentrations of point defects are sensitive to pressure in the lower pressure range, suggesting an effective routine to manipulate point defects in ZrC. The nearest neighbor defect pair is the most stable at high pressure. The insights from our first-principles calculations might be helpful in material design and defects engineering for ZrC-based materials and its applications.

## 1. Introduction

ZrC ceramic, with B1 structure, is characterized by high melting point, extreme stiffness, excellent wear resistance and chemical inertness [1]. Therefore, ZrC is an ideal candidate for applications under extreme conditions, such as high temperature and high pressure. ZrC is widely used in aircraft as structural parts [2], in cutting tools as dispersion hardening particles [3], in microelectromechanical devices as wear-resistant coatings, and especially in high power density reactors at high temperature as a promising fuel-cladding material [4].

ZrC exhibits outstanding physical and chemical properties. The unusual combination of these properties can be traced back to its unique bonding character that the carbide actually a mixture of metallic, covalent, and ionic bonds [5], among which the covalent nature is dominant. As reported, the finite density of state at the Fermi level  $E_F$  and the hybridization of C-p-Zr-d provide evidence for metallic and covalent bonding in ZrC respectively [6,7], and ionic bonding can also be revealed from charge density plots [8]. In addition, some analyses on the properties of stoichiometric ZrC have been presented both by theoretical calculations and experiments. However, as a sub-stoichiometric

compound, ZrC can accommodate a large quantity of point defects, especially carbon vacancies, and maintain stability. There is no systemic investigation for the properties of ZrC with various defects, and so, it is deserved further explorations.

To improve the safety and reliability of nuclear energy systems, the kernel components in future fourth-generation nuclear reactors are required to withstand higher working temperature and more intensive radiation, which gives rise to severe challenges to traditional nuclear materials [9]. In the atomic energy industry, the fuel particles in high-temperature gas-cooled reactors are usually coated by using SiC. To ensure the performance and safety of the coating, the temperature of the coated particles should be controlled below 1600 °C [10], beyond which the fission product retention capacity of SiC will be obviously weakened and the mechanical properties will quickly decline because the SiC coating undergoes thermal decomposition and a phase transition at higher temperatures. ZrC has excellent high temperature performance which potentially meets the requisites to replace SiC as an important component of structural materials in extreme environments.

As a potential candidate material for fuel application in advanced high-temperature reactors, ZrC exposed to radiation environments will

\* Corresponding author.

E-mail address: [ouyangyf@gxu.edu.cn](mailto:ouyangyf@gxu.edu.cn) (Y. Ouyang).

inevitably face the challenging issues of defect generation, migration and aggregation. It is notable to study the possible mechanical and thermophysical response of ZrC under high pressure and high temperature conditions, and the influence induced by the introduction of various point defects, which may ultimately deteriorate the properties and alter its performance. Researches on ZrC with point defects at high temperature and pressure can help to understand the performance at extreme conditions. To our knowledge, there are a series of studies that focused on point defect formation and stability [11–19], but few of them involved the influence of temperature and/or pressure. Mellan *et al.* [20] have explored the formations and concentrations of several types of carbon Frenkel pairs by considering the effect of temperature with ideal solution models. Therefore, the motivation of the present work is to study systematically the structural and thermophysical properties of the pristine and defective ZrC under different temperatures and pressures. The formation abilities and concentrations of point defects, and their interactions for several defect complexes affected by temperature and pressure will be revealed and discussed.

The organization of this paper is as follows. The details of DFT calculation including the associated parameters set and the methodology of the quasi-harmonic Debye model are given in Section 2. In Section 3, the results of the structural and thermophysical properties of the pristine and defective ZrC are presented. And then the defect formation, concentration and interaction are analyzed in detail. Finally, a summary is given in Section 4.

## 2. Methods

As per the research on constructing point defect configurations with different supercell sizes of Yang *et al.* [16], a supercell of pristine ZrC was constructed with a conventional unit cell (8 atoms) as a repeating unit and a  $2 \times 2 \times 2$  repetition pattern. Total energy calculations of perfect or defective ZrC were carried out using the projector-augmented-wave (PAW) method [21] as implemented in the Vienna *ab initio* simulation package (VASP) [22] within the framework of the DFT. The exchange-correlation effects were treated using the generalized gradient approximation (GGA) in the Perdew, Burke and Enzerhof (PBE) [23] parameterization. The planewave basis had an energy cutoff of 600 eV. The Methfessel-Paxton [24] scheme was selected with a smearing width of 0.2 eV. The  $6 \times 6 \times 6$  and  $7 \times 7 \times 7$   $k$ -meshes for the Brillouin zone integration were used for ion relaxation and static calculations, respectively. For the ion relaxation, the convergence criteria for total energies were  $1.0 \times 10^{-5}$  eV, and the maximum force on each atom was  $< 0.02$  eV/Å. A higher energy convergence criterion  $1.0 \times 10^{-6}$  eV was used for a more accurate static energy calculation.

Within the framework of quasi-harmonic approximation, Gibbs2 [25] was used to reveal the thermophysical properties of the solid-phase with pressure and temperature dependence. The Gibbs free energy is expressed as:

$$G^*(V; P, T) = E(V) + PV + F_{vib}(V; T) \quad (1)$$

where  $E(V)$  is the total energy calculated from the perfect or defective ZrC supercell, and  $F_{vib}(V; T)$  is the vibrational Helmholtz free energy, which can be expressed in the following form [26]:

$$F_{vib}(V; T) = nkT \left[ \frac{9}{8} \frac{\theta_D}{T} + 3\ln(1 - e^{\theta_D/T}) - D(\frac{\theta_D}{T}) \right] \quad (2)$$

where  $n$  represents the number of atoms per formula unit (for cubic ZrC,  $n=2$ ),  $k$  is the Boltzmann's constant,  $\theta_D$  is the Debye temperature, and  $D(\theta_D/T)$  is the Debye integral. For  $\theta_D$ , by isotropic approximation, it can be expressed by [27]

$$\theta_D = \frac{\hbar}{k} (6\pi^2 V^{1/2} n)^{1/3} \sqrt{\frac{B_S}{M}} f(\sigma) \quad (3)$$

where  $B_S$  and  $\sigma$  represent the adiabatic bulk modulus and Poisson's ratio of the crystal, respectively,  $M$  is the molar mass of the compound ( $M=103.221$  a.u.), and the expression of  $f(\sigma)$  [28] is

$$f(\sigma) = \left\{ 3 \left[ 2 \left( \frac{2}{3} \frac{1+\sigma}{1-2\sigma} \right)^{3/2} + \left( \frac{1+\sigma}{3(1-\sigma)} \right)^{3/2} \right]^{-1} \right\}^{1/3} \quad (4)$$

For a small range of  $\sigma$  fluctuations (for example, from 0.2 to 0.3), the difference of  $f(\sigma)$  is very small, so  $\theta_D$  is not very sensitive to the value of  $\sigma$ .  $B_S$  is related to  $V$  and  $T$ , and the following approximation was employed to balance calculation requirements and accuracy:

$$B_S \approx B_{sta} = V \left( \frac{d^2 E(V)}{dV^2} \right) \quad (5)$$

where  $B_{sta}$  is the static bulk modulus.

In order to minimize  $G^*$ , a suitable analytical expression namely the thermal equation of state (EOS) is needed. Based on the EOS, the energy and its derivative interpolation can be reliably obtained. The fourth-order Birch-Murnaghan EOS [29] was used to fit the energy-volume ( $E-V$ ) curve, for which the relationship between the pressure and volume can be expressed as:

$$P = \frac{3}{2} B_{T_0} \left[ \left( \frac{V}{V_0} \right)^{\frac{3}{5}} - \left( \frac{V}{V_0} \right)^{\frac{1}{5}} \right] \left\{ 1 + \frac{3}{4} (B'_{T_0} - 4) \left[ \left( \frac{V}{V_0} \right)^{\frac{2}{5}} - 1 \right] + \frac{1}{24} (9B'^2_{T_0} - 63B'_{T_0} + 9B''_{T_0} + 143) \left[ \left( \frac{V}{V_0} \right)^{\frac{2}{5}} - 1 \right]^2 \right\} \quad (6)$$

where  $B_{T_0}$ ,  $B'_{T_0}$  and  $B''_{T_0}$  are the isothermal bulk modulus at standard temperature, its first and second derivative with respect to pressure, respectively. The isothermal bulk modulus  $B_T(T, P)$  can be obtained from the following formula

$$B_T(T, P) = V(T, P) \left( \frac{d^2 G^*(V; T, P)}{dV^2} \right)_T \quad (7)$$

The Poisson's ratio of the defective ZrC is assumed as a constant 0.2 (obtained by averaging several similar experimental results [30–32]). Combined with the thermal EOS, the specific thermophysical quantities such as heat capacity, thermal expansion coefficient, and Gibbs free energy were calculated within a given pressure and temperature range, which can refer to related computations of Hao *et al.* [33] in details.

## 3. Results and discussion

### 3.1. Thermophysical properties of pristine ZrC

The formation energy, defined in terms of the structural energy difference, is used to evaluate the stability of compounds. The formation energy of the ZrC crystal can be expressed as

$$\Delta E_{ZrC} = \frac{1}{m+n} (E_{ZrC} - mE_{Zr} - nE_C) \quad (8)$$

where  $E_{ZrC}$ ,  $E_{Zr}$  and  $E_C$  are the total energy per unit of ZrC, the energy per atom of the hexagonal closed-packed (hcp) Zr, and the energy per atom of the diamond, respectively.  $m$  and  $n$  represent, respectively, the number of Zr and C atoms in the ZrC supercell.

According to Eq. (8), the lattice parameter and formation energy of pristine ZrC from the *ab initio* calculation are shown in Table 1. The comparison indicates that the present lattice constant is in good

**Table 1**

Lattice parameter  $a_0$  (Å) and formation energy  $\Delta E_f$  (eV/atom) of perfect ZrC.

Parameter	Present	Other calculations	Experiments
$a_0$	4.710	4.71 [15] 4.72 [16] 4.725 [19]	4.698 [34] 4.72 [35]
$\Delta E_f$	-0.924	-0.82 [12] -0.84 [16] -0.91 [38]	-1.04 ± 0.03 [36] -0.96 [37]

agreement with other calculations [15,16,19] and experimental values [34,35]. The calculated formation energy is closer to the experimental values [36,37] than the other predictions [12,16,38].

The temperature dependence of the constant volume heat capacity ( $C_V$ ), constant pressure heat capacity ( $C_p$ ) and the volumetric thermal expansion coefficient  $\alpha$  of the pristine ZrC crystal at zero pressure are presented in Fig. 1. The calculated  $C_V$  agrees well with previous theoretical predictions. Compared with other calculations [11,39,40], the present calculated  $C_p$  agrees better with experimental data [41–43]. The present calculated volumetric thermal expansion coefficient is similar as that of Lu *et al.* [44] and is different from the other theoretical predictions [39,45,46], and larger than the experimental results [47].

Fig. 2 demonstrates the behavior of heat capacity varying with temperature under various pressures. From Fig. 2(a) and (c), it can be concluded that with increasing pressure,  $C_V$  and  $C_p$  decrease in the entire temperature range.  $C_V$  tends to be constant under high temperature and high pressure. When the temperature is lower than 500 K, both of  $C_V$  and  $C_p$  increase rapidly as the temperature increases. When the temperature is higher than 1000 K,  $C_V$  increases slowly with temperature and gradually approaches the Dulong-Petit limit at various pressure while  $C_p$  increases significantly as the temperature increases at zero pressure. Fig. 2(b) and (d) show that  $C_V$  and  $C_p$  decrease nonlinearly with the applied pressure at room temperature (300 K).  $C_p$  decreases more rapidly than  $C_V$  does at high temperatures when the pressure increases from 0 GPa to 50 GPa. Therefore, the heat capacity at constant pressure behaviors more differently at a specific temperature and pressure range.

The volumetric thermal expansion coefficients  $\alpha$  of ZrC crystal at four different temperatures depended on pressure are displayed in Fig. 2(f). In the low-temperature range (below 300 K),  $\alpha$  increases rapidly with temperature under low pressure. The slope of  $\alpha$  gradually decreases to zero at higher temperatures.  $\alpha$  decreases nonlinearly with pressure, and it decreases rapidly in the range of 0–50 GPa at various temperatures. The decreased magnitude of  $\alpha$  with the increased pressure at high temperature is larger than that at low temperature. It can be inferred

that the volumetric thermal expansion coefficient of ZrC is sensitive to the small pressure applied and the temperature change below the room temperature.

The pressure-related Debye temperature infers the mechanical stiffened bulk modulus, and thermal softening of bulk modulus corresponds to bond expansion and bond weakening caused by thermal stress in ZrC [48]. Table 2 summarizes the static bulk modulus and Debye temperature calculated from static data. The comparison shows that the calculated bulk modulus and Debye temperature of ZrC are in accordance with those of other calculations [11,18,20,44,49–51] and experiments [30,31,52–55].

Taking the temperature effect into account, the calculated isothermal bulk modulus  $B_T$  and Debye temperature  $\theta_D$ , as functions of temperature and pressure, are illustrated in Fig. 3. The isothermal bulk modulus is suppressed with the increased temperature under various pressures. The decrease is almost linear. Opposite the effect of temperature, it is obvious that  $B_T$  increases significantly with pressure.

Similarly, the Debye temperature  $\theta_D$  of ZrC decreases with increasing temperatures, as illustrated in Fig. 3(c)(d). Especially under low-pressure conditions,  $\theta_D$  decreases rapidly. Moreover, the higher the pressure, the decreasing amplitude will gradually decline.  $\theta_D$  increases significantly with the increased pressure and its rate of increment, as shown in Fig. 3(d), decreases gradually. This means that  $\theta_D$  increases more obviously at the low-pressure range and increases more slowly under high pressure.

### 3.2. Point defects in ZrC

#### 3.2.1. Defective configurations

The defects can be classified into two categories: single defect and defect complex. Single defect includes mono-vacancy, mono-interstitial, and mono-antisite defect, among which the interstitial defect configurations of C are subdivided (approximately) for the different low-index crystal orientations determined by the location of the C–C bond. The defect complex includes the defect pairs that can be assembled from two single defects, including Schottky pairs (SP) composed of a Zr vacancy and a C vacancy, Frenkel pairs (FP), and antisite pairs (AP). For the further study on interactions and ordering of carbon vacancies, we have classified the divacancy of carbon ( $DV_C$ ) as a defect complex. The pair of point defects can be subdivided into two subcategories of strong bonding (SB) and weak bonding (WB) due to their separations in the supercell. When the two defects are the nearest neighbors, the interaction between the defects is usually strong. If the structural stability is taken into account, leaving the two defects as far as possible, the interaction between the two defects would be relatively weakened, which is a representative intermediate state between the two states of strong interaction and isolation. The systems with point defects were constructed based on a 64-atom supercell. In order to determine the size effect of the supercell, a larger supercell with 216 atoms was also used for carbon divacancy. The main results remain the same for the regularity of interaction between the two vacancies up to the fifth nearest neighbor. With the compromise of the computing demands, we have used the model of a 64-atom supercell in this study.

Following the scheme of Razumovskiy *et al.* [13], we found that the strongly bonded Frenkel pair ( $\{FP_{Zr}\}_{SB}$ ) assembled by the zirconium vacancy and the zirconium atom on the nearest neighbor tetrahedral interstitial site is unstable. The nearest neighbor antisite pair ( $\{AP\}_{SB}$ ) is also unstable. Two main factors may cause the final relaxed configuration of the two Zr-related defect pairs to deviate seriously from the initial target configurations. One factor is that the zirconium interstitial atom is too close to the normal lattice site. The other factor is that the Zr atom on the substituted C lattice site is subjected to considerable directional forces provided by the surrounding atoms.

The studies of C interstitial defects [12–14] and C Frenkel defects [20] indicate that the defect configurations associated with C interstitial defects are quite abundant. Interstitial C atom with small atomic radii

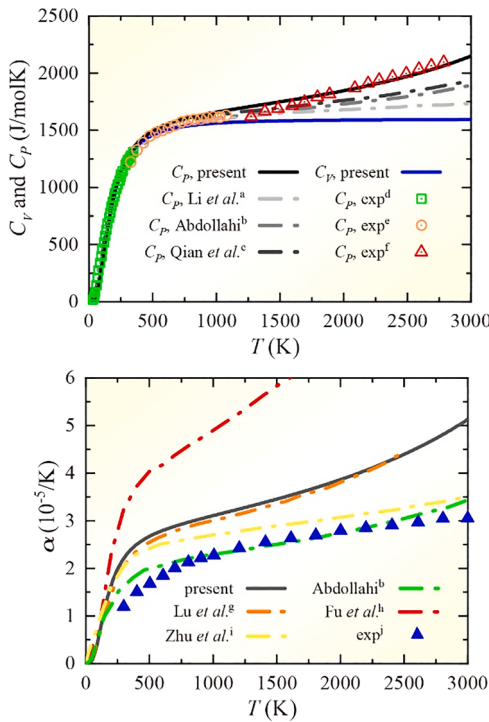


**Fig. 1.** Heat capacity  $C_V$ ,  $C_p$  and thermal volume expansion coefficient  $\alpha$  versus temperature for pristine ZrC. <sup>a</sup>Ref. [11]. <sup>b</sup>Ref. [39]. <sup>c</sup>Ref. [40]. <sup>d</sup>Ref. [41]. <sup>e</sup>Ref. [42]. <sup>f</sup>Ref. [43]. <sup>g</sup>Ref. [44]. <sup>h</sup>Ref. [45]. <sup>i</sup>Ref. [46]. <sup>j</sup>Ref. [47].

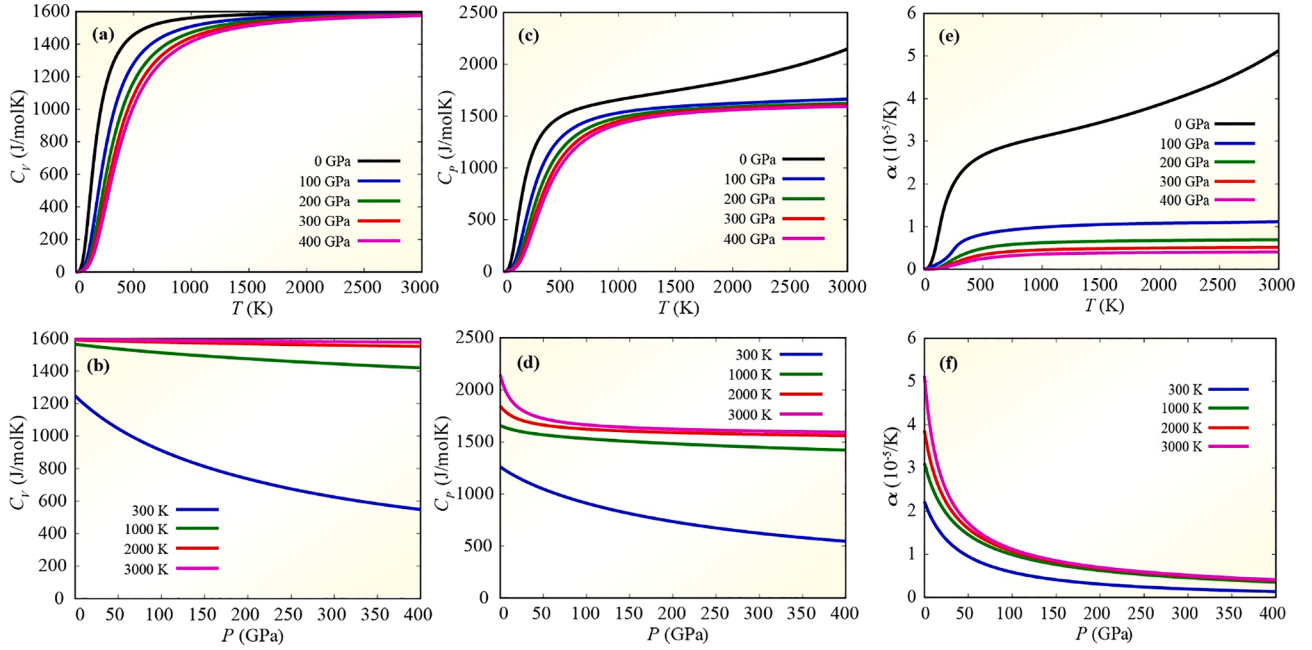


**Fig. 2.** The variations of heat capacity and thermal volume expansion coefficient with temperature and pressure. (a)(c)(e) with temperature at various pressures; (b)(d)(f) with pressures at various temperatures.

**Table 2**

Computed static bulk modulus  $B_0$  (GPa) and the Debye temperature  $\theta_D$  (K) of perfect ZrC.

Properties	Present work	Other calculations	Experiments
$B_0$	221.5	232.2 <sub>PBE</sub> [18], 236.2 <sub>LDA</sub> [20], 221.8 <sub>PBE</sub> [49], 219 <sub>PBE</sub> [50]	208.7 [30], 223 [31], 220 [52]
$\theta_D$	700.9	747 [11], 672 [18], 703 [44], 700 [51]	649 [53], 699 [54], 713.8 [55]

The data calculated using different exchange-correlation functionals are attached with the subscript LDA or PBE.

tends to locate in various interstitial positions. We primarily considered the interstitial structures in which the C-C bond is (approximately) aligned with the three low-index crystal directions [100], [101] and [111]. The interstitial C atoms form carbon dimers, trimers, tetramers, and even pentamers with other nearest neighbor one or more C atoms, as shown in Fig. 4(a), (b), (c), and (d) respectively. In Fig. 4(d), the C atom is located in a double-tetrahedral interstitial site. It bonds to each C atom on the apex of the carbon tetrahedron to form a carbon pentamer ( $I_{C-}[111]_5$ ). When the C atom is disturbed and moves toward a tetrahedral apex atom of Zr, the C-C bond with C atom in the opposite direction will be broken, forming a tetramer ( $I_{C-[111]_4$ ).

By taking the carbon atom from one lattice site as the nearby

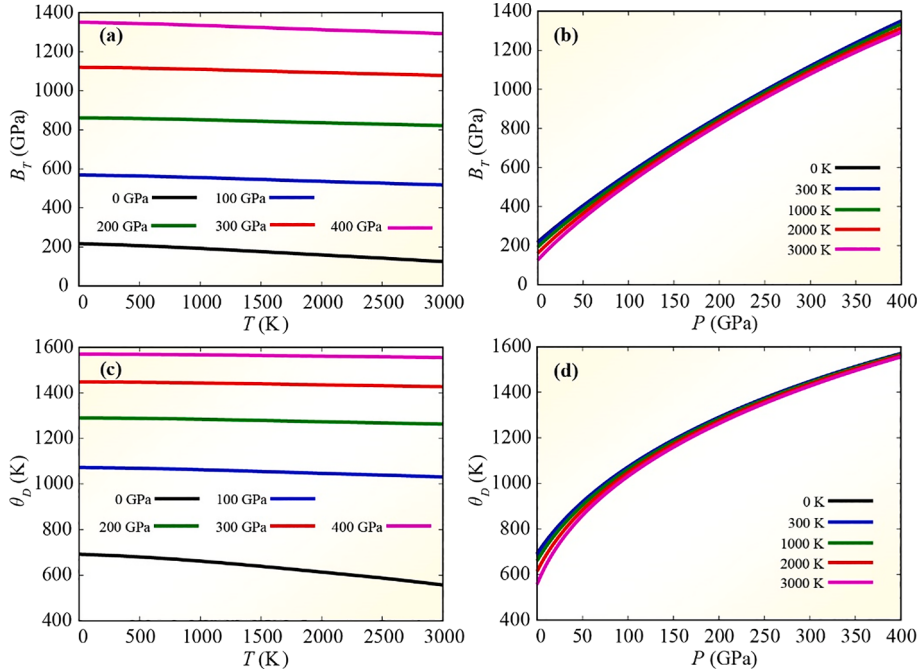


**Fig. 3.** The dependence of isothermal bulk modulus  $B_T$  and Debye temperature  $\theta_D$  on temperature and pressure.

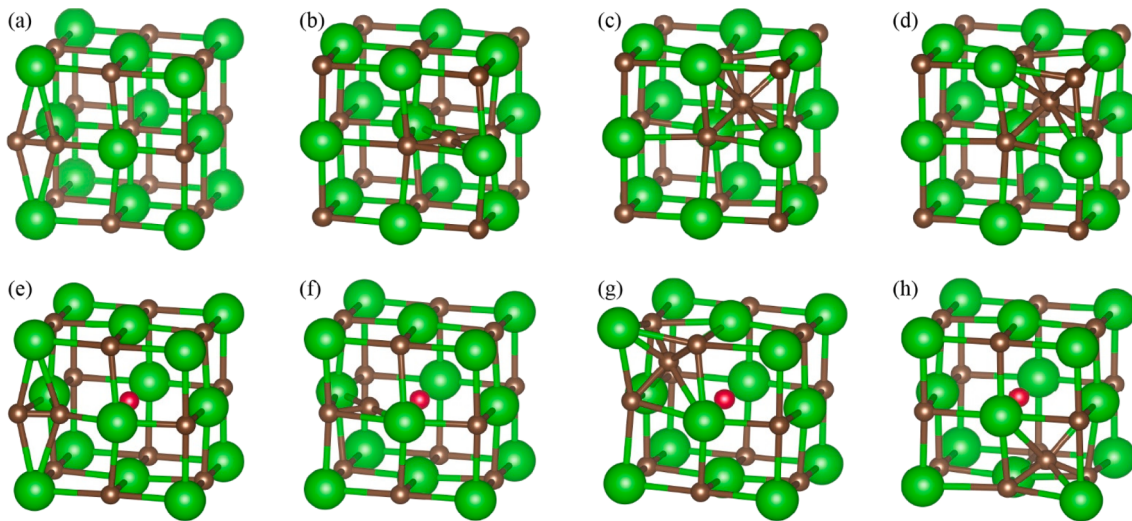


**Fig. 4.** Various carbon mono-interstitials and strongly bonded Frenkel pairs. For each defect structure, the eighth of the supercell that contains the interstitial atom is visualized, where carbon atoms, zirconium atoms, and the vacant carbon site are colored brown, green, and highlighted red, respectively.

interstitial atom, we constructed strongly bonded C-Frenkel pairs as shown in Fig. 4(e), (f) and (g), respectively. If the C atom located in the tetrahedral interstitial site and adjacent to the C vacancy moves toward the midpoint of the two diagonal C atoms, an angular C trimer will be formed, namely forming a strong bonding Frenkel pair ( $\{\text{FP}_{\text{C}}[1\bar{1}1]_3\}_{\text{SB}}$ ) (see Fig. 4(h)). Furthermore, we found that this horned carbon trimer is unstable when in isolation or even weakly bonded to the C vacancy. The C interstitial atom is easily “pulled back” to the linear structure by the two diagonal C atoms on the lattice site. Due to the existence of the C vacancy, the C interstitial at a certain distance from the C vacancy tends to slightly deviate from the regular tetrahedral interstitial site. This phenomenon indicates that the interstitial C atom is disturbed and moves toward the Zr atom located at the corner, and then a C tetrumer corresponding to a weakly bonded Frenkel pair ( $\{\text{FP}_{\text{C}}[1\bar{1}1]_4\}_{\text{WB}}$ ) will be formed.

It is unstable for the strongly bonded Frenkel pairs assembled by a C vacancy and a C interstitial atom that aligns the C-C bond with the [100] and [101] crystal orientations ( $\{\text{FP}_{\text{C}}[100]_2\}_{\text{SB}}$  and  $\{\text{FP}_{\text{C}}[101]_2\}_{\text{SB}}$ ) under high pressure. Moreover, it is interesting that the C interstitial atom in the  $\{\text{FP}_{\text{C}}[100]_2\}_{\text{SB}}$  defect gradually approaches the vacancy with the increase of pressure. Firstly, it reaches the midpoint of the two diagonal Zr atoms, and the resulting C-C dimer is aligned with the [101] crystal orientation. Then, the defect transforms into an  $\{\text{FP}_{\text{C}}[101]_2\}_{\text{SB}}$  type. With pressure increases even more, the interstitial atom would break through the “clamping” effect of the two Zr atoms and move into the vacancy, resulting in a perfect lattice site ultimately.

### 3.2.2. Defect formation energies from *ab initio* calculations

The total energy of a perfect or defective ZrC at 0 K and 0 GPa could be obtained by *ab initio* calculations, based on which the formation energy for various defects is given by the following expression:

$$E_f = E_{\text{def}} - E_{\text{perf}} - \sum_i \Delta n_i \mu_i \quad (9)$$

where  $E_{\text{def}}$  and  $E_{\text{perf}}$  represent the total energy of a defective supercell and the total energy of a perfect supercell with the same size, respectively.  $\Delta n_i$  represents the relative change in the number of atoms of  $i$  (C or Zr) in a defective cell.  $\mu_i$  is the chemical potential of C or Zr, and expressed by the energy per atom calculated by taking the diamond C phase and the hcp Zr phase as the reference states.

The formation energies, defined by Eq. (9), for the considered defects are presented in Table 3. One can see that the calculated formation energies agree well with those in literatures [11–14,16–18,20]. The

formation energies of C vacancies are lower than those of other defects, which is consistent with the fact that ZrC sub-stoichiometric compound with a large number of C vacancies can maintain its stability. While the calculated formation energies of Zr-related defects are all larger than 8 eV/defect. When the formation energy is larger than 5 eV/defect, the defect concentration will be  $< 1 \text{ cm}^{-3}$  even at the temperature of 1000 K [56], which indicates that they are very difficult to form even at high temperatures. The formation energies of C interstitial defects and C Frenkel pairs are between 3 eV/defect and 5 eV/defect.

Comparison of the formation energies for various mono-interstitials of carbon concludes that the C-C-C linear trimer formed by the alignment of the C-C bond with the [101] crystal orientation is the most energetically favorable interstitial configuration. The C pentamer formed by the C atom located in the double-tetrahedron interstitial site is much more difficult to form than the others. The formation energy of the C Frenkel defect pair is relatively lower when the interstitial atom is close to the C vacancy and higher when they are separated by a certain distance. Therefore, the strong bonding state of the Frenkel defect pair is more energetically advantageous than the weak bonding state. In either state, the stability of these Frenkel pair configurations decreases according to the C-C bond aligned along the crystal orientations [111], [101] and [100]. Among them, the configuration of C vacancy with an adjacent angular C trimer is the most favorable in energy.

As for the defect pairs of carbon divacancy, the formation energy of the strongly bonded state is slightly higher than that of the weakly bonded. This may result from the slight repulsion between the two vacancies close to each other. Moreover, the formation energy difference between them is much smaller than that of other defect pairs. Our result suggests that there is a little difference in the possibility of vacancies appearing in the nearest and far away locations.

From Table 3 and Fig. 5, one can conclude that C vacancies are easily formed in ZrC crystals followed by C interstitial atoms and C Frenkel pairs, while Zr-related defects are difficult to be observed due to their much higher formation energies.

### 3.2.3. Bulk modulus and Debye temperature

The static bulk modulus and Debye temperature of the defective ZrC are summarized in Table 4. Compared with Table 2, the bulk moduli of defective ZrC are generally smaller than the previous results calculated by Jiang *et al.* [18] and Mellan *et al.* [20] (about 10 GPa smaller than Jiang’s and about 15 GPa smaller than Mellan’s). One of the reasons is that Mellan *et al.* used the LDA functional, which is different from the GGA-PBE functional used in most studies and present calculations, while

**Table 3**

The formation energies of various point defects in ZrC.

Classification	Defect structures	Description	$E_f$ (eV/defect)	Other cals.
Single point	$V_C$	C mono vacancy	1.13	1.16 [11], 1.08 [18]
	$V_{Zr}$	Zr mono vacancy	8.89	8.98 [11], 8.89 [18]
	$I_{C-[100]_2}$	C dimer	3.80	<sup>a</sup> 4.43 [12], 4.39 [14]
	$I_{C-[101]_3}$	C linear trimer	3.18	3.52 [14], 3.56 [17]
	$I_{C-[111]_5}$	C pentamer	4.83	3.61 [16]
	$I_{C-[111]_4}$	C tetramer	3.50	3.82 [12], 3.98 [14]
	$I_{Zr}$	Zr occupies the tetrahedral site	8.37	8.80 [16], 8.01 [18]
	$C_{Zr}$	C occupies Zr lattice site	12.82	12.97 [14], 13.28 [18]
	$Zr_C$	Zr occupies C lattice site	9.73	9.65 [14], 9.56 [18]
	$\{DV_C\}_{SB}$	Nearest C divacancy	2.34	–
	$\{DV_C\}_{WB}$	Dissociated C divacancy	2.29	–
	$\{SP\}_{SB}$	Nearest C-Zr divacancy	8.40	<sup>b</sup> 8.33 [11], <sup>b</sup> 6.53(6.55) [13]
Complex	$\{SP\}_{WB}$	Dissociated C-Zr divacancy	10.01	<sup>b</sup> 8.02(8.16) [13], <sup>c</sup> 8.14 (8.17) [16]
	$\{FP_{C-[100]_2}\}_{SB}$	The C vacancy nears a C dimer	4.40	–
	$\{FP_{C-[100]_2}\}_{WB}$	Dissociated C vacancy and C dimer	4.93	4.436 [20]
	$\{FP_{C-[101]_2}\}_{SB}$	C dimer nears and points to the C vacancy	4.005	–
	$\{FP_{C-[101]_3}\}_{WB}$	Dissociated C vacancy and linear C trimer	4.33	4.335 [20]
	$\{FP_{C-[111]_4}\}_{SB}$	The C vacancy nears a C tetramer	4.01	–
	$\{FP_{C-[111]_4}\}_{WB}$	Dissociated C vacancy and C tetramer	4.54	<sup>d</sup> 4.54(4.11) [16], 4.441 [20]
	$\{FP_{C-[111]_3}\}_{SB}$	The C vacancy nears an angular C trimer	3.44	3.247 [20]
	$\{FP_{Zr}\}_{WB}$	Dissociated Zr vacancy and Zr interstitial	17.05	<sup>b</sup> 18.61 [13], <sup>c</sup> 17.69(17.26) [16]
	$\{AP\}_{WB}$	Dissociated antisite pair	18.77	<sup>a</sup> 22.56(22.65) [12]

Data with an alphabetic superscript are calculated using different expression formulas, and the results recalculated with these expressions are shown in parentheses.

Duff *et al.* [57] reported that the LDA functional could improve the performance of the bulk modulus of ZrC crystals. It is obvious that the bulk modulus of defective ZrC is reduced. The reduced magnitude is closely related to the type of defect. The bulk moduli of the configurations containing a C vacancy or various C interstitial defects are quite close to each other. The same similarity can be observed for configurations containing different C-Frenkel pairs. For the former category, the introduction of defects reduces the bulk modulus of ZrC by about 2–7 GPa compared to the pristine crystal. The reduction is relatively small. The introduction of the latter category for C-Frenkel pairs reduces by about 10–14 GPa. On the whole, the C interstitial atom located at the double-tetrahedron interstitial site ( $I_{C-[111]_5}$ ) minimizes the reduction of the bulk modulus. On the contrary, the Zr Frenkel pair and the antisite pair reduce the bulk modulus by about 20 GPa and 32 GPa, respectively, a fairly significant decline. In terms of the relative value of the bulk modulus among various defect configurations, the trend of our results is generally consistent with that of Jiang *et al.* [18] and Mellan *et al.* [20].

The Debye temperature of ZrC is lower than that of SiC (the experimental Debye temperature 1123 K [58]). Our prediction of the Debye temperature for the perfect ZrC crystal is very close to those of the most theoretical calculations and experiments. While for the configuration containing defects, few data are available in the literatures. The predicted results provided by Jiang *et al.* [18] are generally smaller than those of our calculations. For the defect configuration that the C interstitial atom is located in the double-tetrahedron interstitial site ( $I_{C-[111]_5}$ ), the Debye temperature is slightly higher than that of the perfect lattice, or almost equal (it is also true for the prediction of Jiang *et al.* [18]). As for the other cases, the introduction of defects reduces the

**Table 4**

The static bulk modulus and the Debye temperature of defective ZrC system.

Perfect/Defective	$B_0$ (GPa)	Previous work	$\theta_D$ (K)	Previous work
$V_C$	214.4	224.9 <sub>PBE</sub> [18]	687.2	682.5 [18]
$V_{Zr}$	214.3	222.0 <sub>PBE</sub> [18]	695.3	657.3 [18]
$I_{C-[100]_2}$	216.2	–	696.6	–
$I_{C-[101]_3}$	214.2	–	693.0	–
$I_{C-[111]_5}$	219.6	230.7 <sub>PBE</sub> [18]	701.0	676.7 [18]
$I_{C-[111]_4}$	216.9	–	696.8	–
$I_{Zr}$	206.0	212.9 <sub>PBE</sub> [18]	674.1	644.2 [18]
$C_{Zr}$	214.7	225.1 <sub>PBE</sub> [18]	698.2	666.2 [18]
$Zr_C$	204.6	214.3 <sub>PBE</sub> [18]	668.3	589.2 [18]
$\{DV_C\}_{SB}$	207.0	–	673.1	–
$\{DV_C\}_{WB}$	209.4	–	676.8	–
$\{SP\}_{SB}$	205.6	–	679.6	–
$\{SP\}_{WB}$	206.1	–	680.3	–
$\{FP_{C-[100]_2}\}_{WB}$	210.7	225.1 <sub>LDA</sub> [20]	685.5	–
$\{FP_{C-[101]_3}\}_{WB}$	207.8	218.8 <sub>LDA</sub> [20]	680.3	–
$\{FP_{C-[111]_4}\}_{SB}$	211.5	–	685.8	–
$\{FP_{C-[111]_4}\}_{WB}$	209.2	225.2 <sub>LDA</sub> [20]	682.2	–
$\{FP_{C-[111]_3}\}_{SB}$	209.6	226.8 <sub>LDA</sub> [20]	683.0	–
$\{FP_{Zr}\}_{WB}$	201.3	–	672.3	–
$\{AP\}_{WB}$	189.9	–	651.9	–

The data calculated using different exchange-correlation functionals are attached with the subscript of <sub>LDA</sub> or <sub>PBE</sub>.

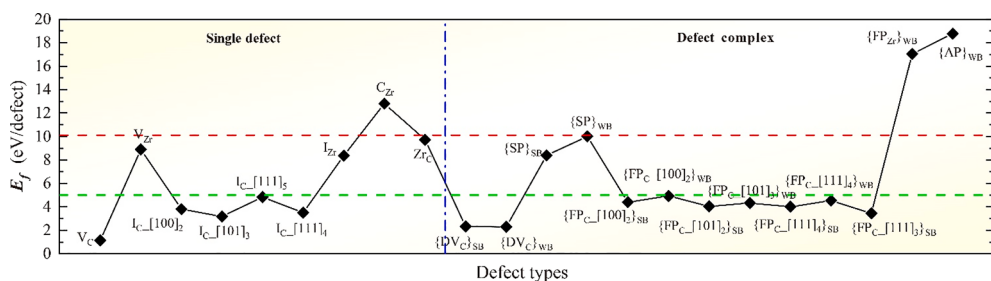


**Fig. 5.** The relative trend chart of the formation energy of various defects. The two categories of defects are distinguished by a blue dash-dot line, and the formation energies of all defects can be divided into three levels by two dashed lines colored green and red respectively.

Debye temperature, but the decrement is smaller than those provided by them.  $Zr_C$  antisite defect has the most obvious negative effect on Debye temperature among all the point defects. The calculations of Jiang *et al.* [18] show that the introduction of C vacancies slightly increases the Debye temperature, while our result exhibits a negative effect, just as same as the other defects. The Debye temperature of the ZrC configurations with the carbon divacancy is more reduced compared with that of the monovacancy, which means that the negative effect should be more convincing.

The bulk modulus and Debye temperature of the ZrC configuration with defect pairs are generally lower than those of single-point defects, which indicates that the accumulation of defects has a more profound effect on the thermophysical properties of ZrC. For the vacancy pairs, including carbon divacancies and Schottky pairs, the reduction of bulk modulus and Debye temperature for the strong bonding state is slightly more obvious than that for the weak bonding state, which means that the aggregation of vacancies in ZrC containing a certain quantity of vacancies is more detrimental to the bulk modulus and Debye temperature. Generally, a lower bulk modulus corresponds to a lower Debye temperature. The introduction of carbon vacancies seems to cause the Debye temperature to be furtherly declined.

### 3.2.4. Gibbs energy of defect formation

The Gibbs energy for the defect formation is

$$\Delta G_f = G_{def} - G_{perf} - \sum_i \Delta n_i G_i \quad (10)$$

where  $G_{def}$  and  $G_{perf}$  are Gibbs free energies of the defective supercell and the perfect supercell, respectively, and  $G_i$  is the Gibbs free energy per atom in diamond crystal or hcp Zr crystal.

For the fairly high defect formation energies from *ab initio* calculations of  $C_{Zr}$ ,  $\{FP_{Zr}\}_{WB}$ , and  $\{AP\}_{WB}$ , even the effects of temperature and pressure are included, there is no significant change, which means that the appearance of the three defects in the entire temperature and pressure range is almost impossible.

Firstly, the behaviors of C vacancies and C interstitials with lower formation energy in a certain temperature and pressure range are discussed. The contour maps (with a gradient of 50 or 100 kJ/mol) of Gibbs energy of formation are respectively shown in Figs. 6 and 7. The contours in Fig. 6 are much flatter than those in Fig. 7. This means that the Gibbs energy of formation for C vacancies in ZrC is much less affected by temperature than that for C interstitial defects. At some pressures, the Gibbs energy of formation for C vacancies decreases non-monotonously with increasing temperature, and sometimes it even slightly increases. However, the Gibbs energy of formation for C interstitials decreases with the increase of temperature at all pressure ranges. Except for the  $I_{C-[100]_2}$  configuration, which has a large fluctuation (about 600 kJ/mol), the energy fluctuation range of other C interstitial configurations is similar to that of a C mono vacancy, about 300 kJ/mol. In the low

pressure range (<50 GPa), the Gibbs energies of formation for C vacancies and two carbon interstitial defects,  $I_{C-[100]_2}$  and  $I_{C-[101]_3}$ , increase rapidly with the increase of pressure, which means that they would be suppressed by applying a smaller pressure.

At the same temperature, the Gibbs energies of formation for C vacancies and  $I_{C-[101]_3}$  defect have a clear trend of increasing firstly and then decreasing with the pressure. It changes slowly in a considerable pressure range near the summit, which will lead to a large “relative forbidden zone” for the formation of defects. When the pressure reaches to an ultra-high level, the effect of pressure on the formation of these defects turns from negative to positive. It is worth notable that the contour maps describing the formation of C interstitial defects have obvious characteristics. For  $I_{C-[100]_2}$  defects, the Gibbs energy of formation increases with pressure throughout the entire pressure range. This means that the higher the pressure, the less conducive to the formation of the defects. As for  $I_{C-[111]_5}$  and  $I_{C-[111]_4}$  defects, as the pressure increases, the Gibbs energies of formation firstly have a small increment in the low-pressure range. Then it decreases approximately linearly until 400 GPa, which results in the Gibbs energies of formation of the high-pressure range being even smaller than that of the low-pressure. The high-temperature and high-pressure likely are of benefit to the forming of the two types of defects.

The contour maps of Gibbs energy for carbon Frenkel pair formation varied with temperature and pressure are shown in Fig. 8 (contour increment with a gradient of 100 kJ/mol). The Gibbs energies of formation for all defects increase rapidly with the pressure in the low-pressure range followed by a large-width peak, and then a slow decrease in the ultra-high-pressure region. This indicates that the effects of pressure on the formation energies of all the defects turn from negative to positive when the pressure increases. For the considered pressures, the Gibbs energies of formation of all defects decrease significantly with increasing temperature. At a certain temperature, similar to that for the C interstitial defect  $I_{C-[100]_2}$ , the Gibbs energy of formation for  $\{FP_{C-[100]_2\}_{WB}}$  defect has the largest variation (870 kJ/mol) throughout the pressure range, then followed by the  $\{FP_{C-[101]_3\}_{WB}}$  (624 kJ/mol), but the variations for the others are small (about 400 kJ/mol). From the Gibbs energy of formation, all the Frenkel pairs are relatively easily formed at low pressure and high temperature. For  $\{FP_{C-[100]_2\}_{WB}}$  defects, the minimum of Gibbs energy of formation in ultra-high pressure zone is significantly higher than that in low pressure zone (about 700 kJ/mol), which means that it is extremely difficult to form in the high pressure region.

Finally, the contours of Gibbs energies of formation varied with pressure and temperature for five Zr-related defects are demonstrated in Fig. 9. These defects have high Gibbs energies of formation throughout the temperature and pressure range, suggesting that the formations of these defects are more difficult. The Gibbs energies of formation for  $V_{Zr}$ ,  $\{SP\}_{SB}$  and  $\{SP\}_{WB}$  defects increase fairly rapidly with pressure in the low pressure range. For zirconium interstitial defects ( $I_{Zr}$ ), it increases

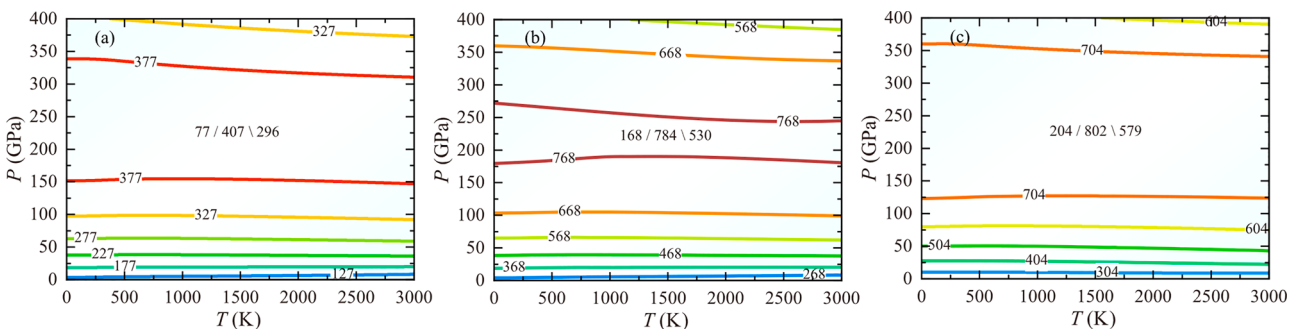


**Fig. 6.** Gibbs energies of formation, with the unit kJ/mol, of carbon vacancies vary with temperature and pressure. (a) carbon mono vacancy; (b) strongly bonded carbon divacancy; (c) weakly bonded carbon divacancy. The minimum of formation energy at zero pressure, the global maximum, and the minimum at ultra-high pressure are separated by “/” and “\” in turn, which is located at the region of high formation energy.

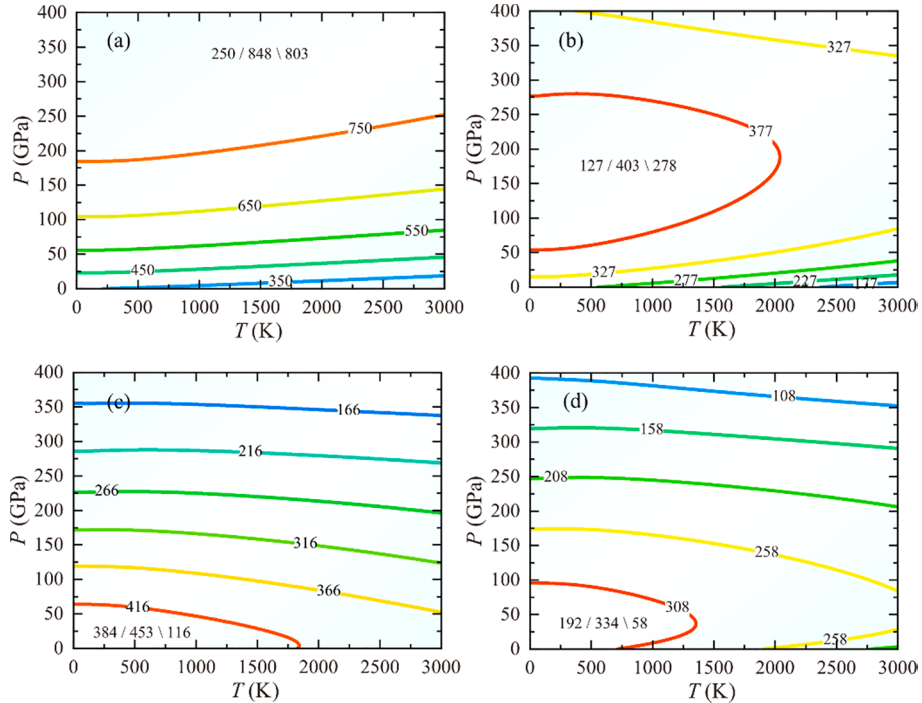


**Fig. 7.** Gibbs energies of formation for carbon interstitials in ZrC vary with the temperature and pressure. (a)–(d) correspond to  $I_{C-[1\ 0\ 0]_2}$ ,  $I_{C-[1\ 0\ 1]_3}$ ,  $I_{C-[1\ 1\ 1]_5}$ , and  $I_{C-[1\ 1\ 1]_4}$  respectively.

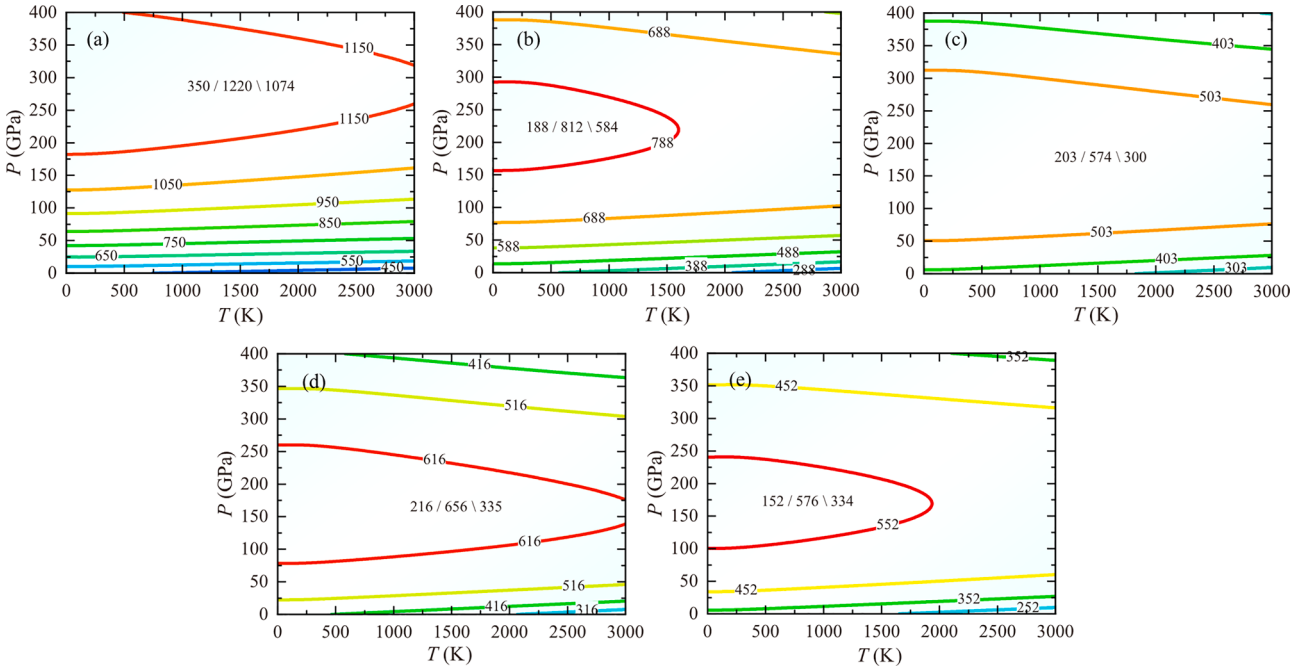


**Fig. 8.** Gibbs energies of formation for carbon Frankel defect pairs in ZrC vary with temperature and pressure. (a)–(e) correspond to  $\{FP_{C-[1\ 0\ 0]_2\}_{WB}}$ ,  $\{FP_{C-[1\ 0\ 1]_3\}_{WB}}$ ,  $\{FP_{C-[1\ 1\ 1]_4\}_{SB}}$ ,  $\{FP_{C-[1\ 1\ 1]_4\}_{WB}}$ ,  $\{FP_{C-[1\ 1\ 1]_3\}_{SB}}$  respectively.

monotonously with pressure. For  $Zr_C$  antisite defect it decreases almost linearly after a small increment in low pressure range. The decrement is close to 400 kJ/mol, which results in a minimum in the high pressure and low temperature zone. In the high pressure zone, the Gibbs energy of formation for  $Zr_C$  defect increases abnormally with increasing temperature, and those for  $\{SP\}_{SB}$  and  $\{SP\}_{WB}$  tend to decrease firstly and then increase with temperature in the low pressure range (0–10 GPa). In most other cases, the Gibbs energies of formation decrease with the

temperature.

In order to compare the formation abilities of the same category of defects mentioned above at the same pressure or temperature, their Gibbs energies of formation at 0 K (0 GPa) as functions of pressure (temperature) are plotted in Fig. 10. One can see that the Gibbs energy for the defect formation varies characteristically with pressure or temperature.

For the formation energies of the C mono-vacancy and C mono-

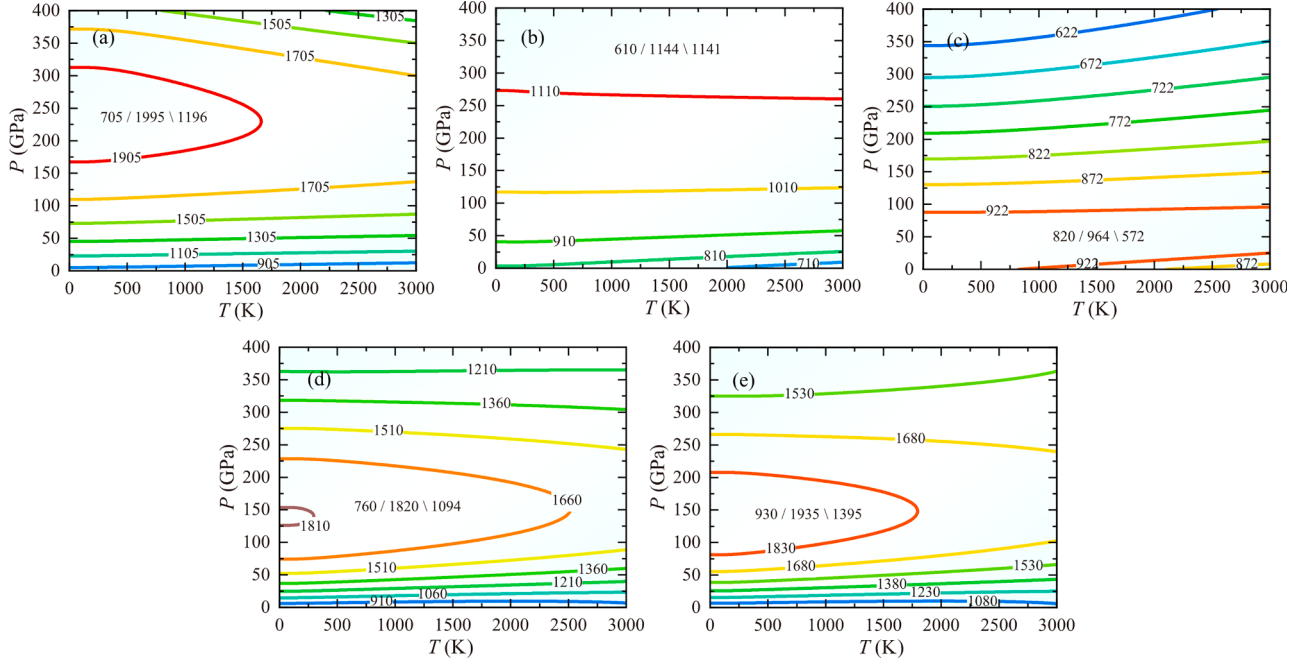


**Fig. 9.** Gibbs energies for 5 types of Zr-related defects formation vary with temperature and pressure. (a)–(e) correspond to  $V_{Zr}$ ,  $I_{Zr}$ ,  $Zr_C$ ,  $\{SP\}_{SB}$ , and  $\{SP\}_{WB}$ , respectively.

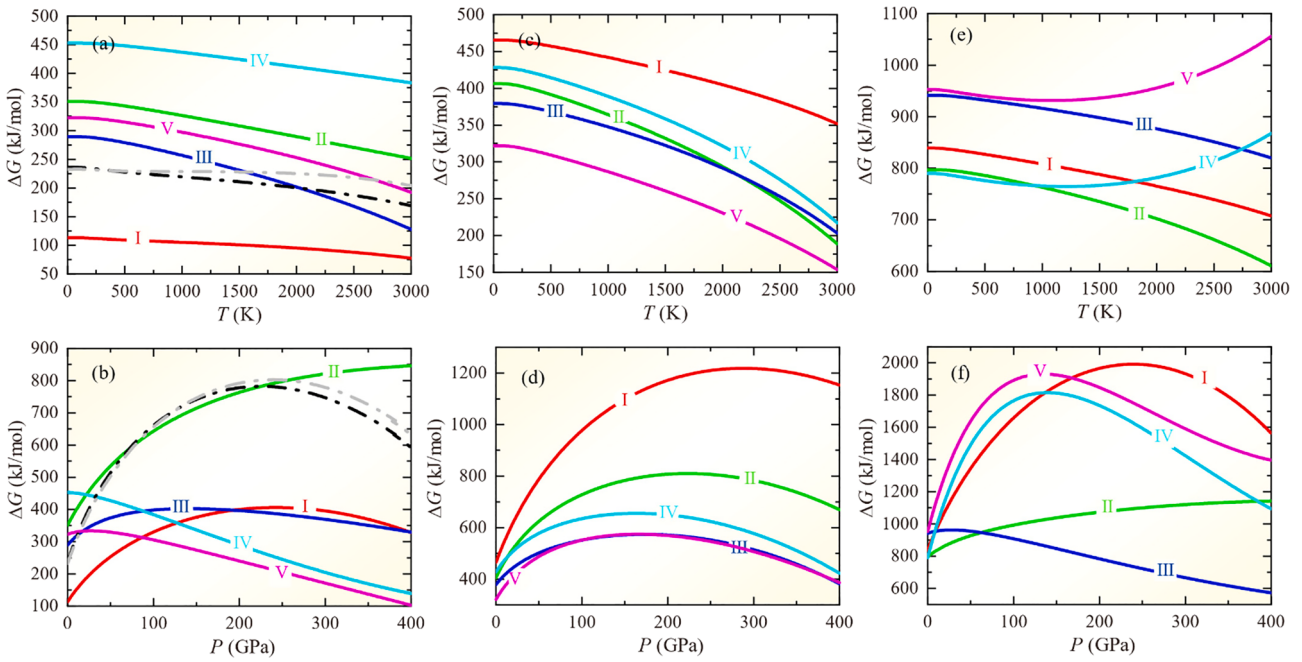


**Fig. 10.** The temperature (pressure) dependencies of Gibbs energy of defect formation at 0 GPa (0 K) after classification. (a) and (b) correspond to carbon vacancies and interstitials, where curves I–V correspond to  $V_C$ ,  $I_C-[100]_2$ ,  $I_C-[101]_3$ ,  $I_C-[111]_5$ , and  $I_C-[111]_4$ , respectively, while the black dash line and gray dash line correspond to  $\{DV_C\}_{SB}$  and  $\{DV_C\}_{WB}$  respectively. (c) and (d) correspond to carbon Frankel defect pairs, where curves I–V correspond to  $\{FP_C-[100]_2\}_{WB}$ ,  $\{FP_C-[101]_3\}_{WB}$ ,  $\{FP_C-[111]_4\}_{SB}$ ,  $\{FP_C-[111]_4\}_{WB}$ , and  $\{FP_C-[111]_3\}_{SB}$ , respectively. (e) and (f) correspond to five types of Zr-related defects, where curves I–V correspond to  $V_{Zr}$ ,  $I_{Zr}$ ,  $Zr_C$ ,  $\{SP\}_{SB}$ ,  $\{SP\}_{WB}$ , respectively.

interstitials, it is the lowest for the mono-vacancy when the pressure is low, while it is the highest for the  $I_C-[111]_5$  defect. Above 100 GPa, the Gibbs energy of formation for  $I_C-[100]_2$  defect is much higher than those of the other single point defects, among which the Gibbs energy of formation for  $I_C-[111]_4$  defect is the lowest. The Gibbs energy for carbon divacancy formation is similar as some interstitial defects under low pressure. However, it increases significantly with the increase of

pressure and is much higher than those of other defects except that of  $I_C-[100]_2$ , which indicates that pressure can effectively reduce the aggregation of isolated C vacancies. At the same temperature, the Gibbs energies of formation for  $\{DV_C\}_{SB}$  and  $\{DV_C\}_{WB}$  are almost equal in the pressure range of 0–150 GPa, but the higher pressure is more unfavorable for  $\{DV_C\}_{WB}$ , indicating that carbon divacancies tend to be tightly bonded under high pressure. In the case of 0 GPa, the Gibbs energy of

formation for each type of defect decreases with the temperature. This phenomenon can be explained by the fact that near the ambient pressure, as the temperature increases, the probability of C atoms left the normal lattice site to form vacancies increase. Then the probability of C vacancies aggregated also increases. At the same time, the lattice expands and the probability of C atoms with a small atomic radius entering each interstitial site increases too. At 0 K, curves IV and V in Fig. 10(b) show that the Gibbs energies of formation for  $I_{C\langle 111 \rangle_5}$  and  $I_{C\langle 111 \rangle_4}$  decrease almost linearly with the increased pressure under high pressure. Curves I and III in Fig. 10(b) are close to each other under high pressure, and this feature remains at other temperatures, which means these two defects show similar forming abilities under high pressure.

When the temperature increases from 0 to 3000 K, the decrements of formation energy are 1.17, 2.25, 1.82, 2.18 and 1.74 eV/defect (corresponding to curves I–V) for C Frenkel pairs  $\{FP_{C\langle 100 \rangle_2}\}_{WB}$ ,  $\{FP_{C\langle 101 \rangle_3}\}_{WB}$ ,  $\{FP_{C\langle 111 \rangle_4}\}_{SB}$ ,  $\{FP_{C\langle 111 \rangle_4}\}_{WB}$ ,  $\{FP_{C\langle 111 \rangle_3}\}_{SB}$ , respectively, at 0 pressure (Fig. 10). The reduction is generally larger than those of C vacancies and C interstitials. The results of Mellan *et al.* [20] for  $\{FP_{C\langle 100 \rangle_2}\}_{WB}$ ,  $\{FP_{C\langle 101 \rangle_3}\}_{WB}$ ,  $\{FP_{C\langle 111 \rangle_4}\}_{WB}$ ,  $\{FP_{C\langle 111 \rangle_3}\}_S$  are about 1.46, 1.10, 1.03 and 0.84 eV/defect, respectively. In the considered pressure range, the Gibbs energy of formation for  $\{FP_{C\langle 100 \rangle_2}\}_{WB}$  is the highest.  $\{FP_{C\langle 111 \rangle_3}\}_{SB}$  has the lowest formation energy at low pressure and  $\{FP_{C\langle 111 \rangle_4}\}_{SB}$  has the lowest formation energy at high pressure, which is consistent with the gradual transition from  $\{FP_{C\langle 111 \rangle_3}\}_{SB}$  to  $\{FP_{C\langle 111 \rangle_4}\}_{SB}$  under compression. Since the C interstitial atoms within  $\{FP_{C\langle 111 \rangle_4}\}_{SB}$  and  $\{FP_{C\langle 111 \rangle_3}\}_{SB}$  configurations are located very close to each other, at the same temperature, curves III and V in Fig. 10(d) almost overlap in the pressure range of 100–400 GPa. With the increase of pressure, the distance between the C interstitial atom and the C vacancy in  $\{FP_{C\langle 111 \rangle_4}\}_{WB}$  defect shortened, the interaction strengthened, so that the curve IV gradually approaches curves III and V under higher pressure.

Unlike the above two categories of defects, the Gibbs energies of formation for Zr-related defects corresponding to curves I–V in Fig. 10(e) usually have abnormal relationships with temperature at different pressures. At 0 GPa, when the temperature increases from 0 to 3000 K, the Gibbs energies of formation for  $V_{Zr}$ ,  $I_{Zr}$ , and  $Zr_C$  reduce by 1.36, 1.93, and 1.26 eV/defect, respectively, while the  $\{SP\}_{SB}$  and  $\{SP\}_{WB}$  defects increase by about 0.80 eV/defect and 1.07 eV/defect respectively after a small decrease. This indicates that the recombination probability of interstitial Zr atoms and vacancies (*i.e.* probability of returning to the normal lattice site) increases significantly as the temperature increases. It can be inferred by that the Gibbs energy for Zr interstitial atoms formation is lower than that for Zr vacancies and decreases more quickly with increasing temperature. As a result, the formation of Schottky pairs would be inhibited. In the range of 0–100 GPa, the Gibbs energy of formation for weakly bonded Schottky pair ( $\{SP\}_{WB}$ ) is the highest, while in the range of 100–400 GPa, that of  $Zr_C$  defect is obviously the lowest.

The volume of the material shrinks by applying pressure. While it usually expanges with temperature, which is equivalent to a negative pressure applied. In the most of cases mentioned above, pressure results in an inhibitory effect on the formation of defects, while the temperature tends to be a favorability of defect formation. The competition between the two effects results in formation ability at high temperature and pressure.

### 3.2.5. Defect concentrations

The equilibrium concentration of defects in the crystal is closely related to the Gibbs energy of defect formation. The Arrhenius relationship can provide an approximate description of the defect concentration in a wider temperature range. Therefore, the relationship between the concentration  $X_j$  for various types of defects and the Gibbs energy of formation  $\Delta G_j$  ( $j$  represents the type of defect) and the temperature  $T$  can be expressed as

$$X_j = e^{-\Delta G_j/kT} \quad (11)$$

As the previous discussion on Gibbs energy of formation, we confirm that it is a wise choice to divide the concentration distribution of various defects into three categories. For C vacancies, C interstitial defects, and C Frenkel pairs, the value of  $10^{-10}$  (concentrations higher than this value are considerable) is set as the lower bound of the concentration distribution. However, since the Gibbs energies of formation for the remaining five Zr-related defects are significantly larger than that for C-related defects, we set a lower bound of  $10^{-20}$ . There is no doubt that the global concentration maximum for each type of defect occurs in the high-temperature zone.

The concentrations of C vacancies and C interstitials predicted by the Arrhenius relationship are shown in Figs. 11 and 12. For C vacancies and two types of C interstitials  $I_{C\langle 100 \rangle_2}$  and  $I_{C\langle 101 \rangle_3}$ , the concentration maximum occurs in the low pressure zone, while the  $I_{C\langle 111 \rangle_5}$  and  $I_{C\langle 111 \rangle_4}$  defects have a much higher concentration in the high-pressure zone, which undoubtedly corresponds to their lower Gibbs energies of formation as mentioned above. At high temperature and under low pressure, the order of concentration maxima for these point defects from lowest to highest are  $I_{C\langle 111 \rangle_5}$ ,  $I_{C\langle 100 \rangle_2}$ ,  $I_{C\langle 111 \rangle_4}$ ,  $I_{C\langle 101 \rangle_3}$  and  $V_C$ . In the high pressure zone,  $I_{C\langle 100 \rangle_2}$  defect has no concentration distribution in the specified range, which is consistent with its Gibbs energy of formation increasing simply with the pressure while the concentration maximum for other defects decreases in the order of  $I_{C\langle 111 \rangle_4}$ ,  $I_{C\langle 111 \rangle_5}$ ,  $I_{C\langle 101 \rangle_3}$  and  $V_C$ , indicating that high temperature and high pressure are very favorable for the formation of C interstitial atoms near the tetrahedral interstitial site. The lower bounds of  $\{DV_C\}_{SB}$  and  $\{DV_C\}_{WB}$  are almost coincident (see the black and gray dash lines in Fig. 12(e)). But since the former is more sensitive to temperature at low pressures, its concentration maximum is larger than that of the latter (corresponding to the maximum marks in Fig. 11(a) and (b)). The concentration distribution range of carbon divacancies is much smaller than that of isolated C vacancies, and there is no concentration distribution higher than the lower bound in a range of high pressure zone. This may be attributed to the inhibitory effect of high pressure on the accumulation of isolated C vacancies. Comparing their maximum concentrations, we infer that the quantity of C vacancies increases and only partially aggregates with the effect of high temperature at low pressures. In Fig. 12(e), curves I and III are close to each other under high pressure, which corresponds to the situation in Fig. 10(b), and also corresponds to concentration distributions of  $V_C$  and  $I_{C\langle 101 \rangle_3}$  defects under high pressure. Under low pressure, except that the concentration of isolated C vacancies is close to the lower bound at about 600 K, the temperature for other point defects concentration near the lower bound is above 1250 K or even higher than 2000 K. Whereas with the effect of ultra-high pressure, as long as about 700 K and 500 K are respectively provided for  $I_{C\langle 111 \rangle_5}$  and  $I_{C\langle 111 \rangle_4}$ , their concentrations can reach the lower bound.

The Gibbs energies of formation for the C-Frenkel pairs are generally larger than that of single C-related point defects. Therefore, the concentration distribution of the former above the lower bound occupies a narrower temperature and pressure zone than the latter, as shown in Fig. 13. For all C-Frenkel pairs, the lower bound of the concentration can only be reached above 1300 K at low or ultrahigh pressure. The global concentration maximum occurs in the low pressure zone. Combining the previous discussions on the Gibbs energy of formation and concentration distributions of  $I_{C\langle 111 \rangle_5}$  and  $I_{C\langle 111 \rangle_4}$  defects, we can conclude that the considerable concentrations of C-Frenkel pairs  $\{FP_{C\langle 111 \rangle_4}\}_{SB}$ ,  $\{FP_{C\langle 111 \rangle_4}\}_{WB}$  and  $\{FP_{C\langle 111 \rangle_3}\}_{SB}$  appear in the high pressure zone but are relatively low, because of the introduction of C interstitial atoms located near the tetrahedral interstitial site and the restriction of carbon vacancies. As for  $\{FP_{C\langle 100 \rangle_2}\}_{WB}$  and  $\{FP_{C\langle 101 \rangle_3}\}_{WB}$  defects, there is only a specified range of concentration distribution under low pressure. In Fig. 13(f), the closely spaced contour curves III and V are close to

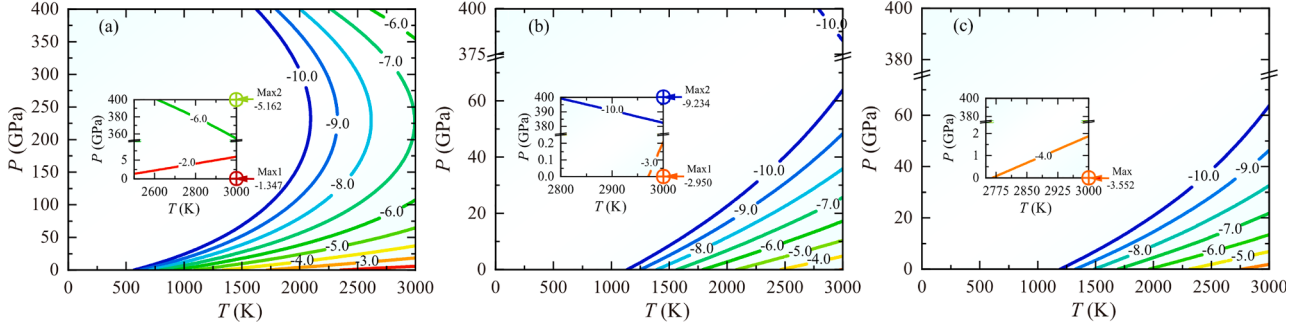


**Fig. 11.** Concentration distribution (log scale) of carbon vacancies over a wide temperature and pressure range. (a)–(c), with the lower concentration bound of  $10^{-10}$ , correspond to  $V_C$ ,  $\{DV_C\}_{SB}$ , and  $\{DV_C\}_{WB}$  respectively. Note, the concentration maximum at 0 GPa or 400 GPa is marked in the illustrations with the colored symbol  $\oplus$ .

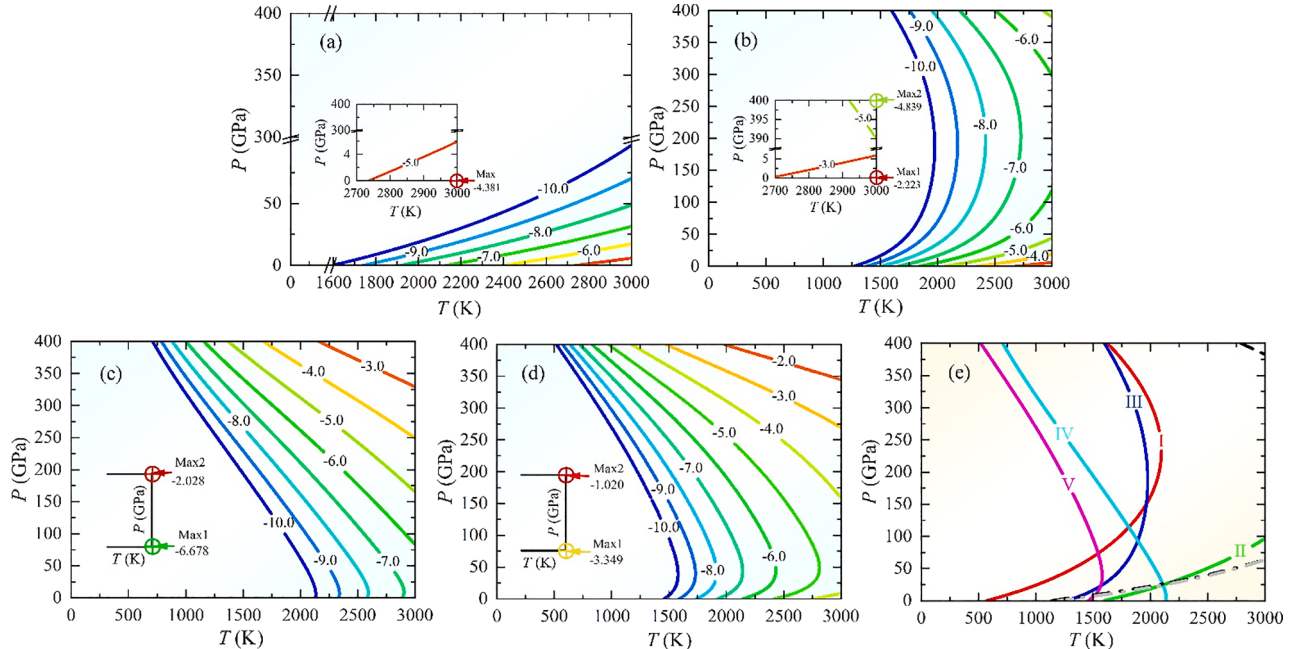


**Fig. 12.** Concentration distribution (log scale) of carbon interstitials over a wide temperature and pressure range. (a)–(d) correspond to  $I_C-[100]_2$ ,  $I_C-[101]_3$ ,  $I_C-[111]_5$  and  $I_C-[111]_4$  respectively, the same sequence curves II–V refer to in (e), where only the lower concentration bounds of carbon vacancies (curve I, the black dash line and the gray dash line correspond to  $V_C$ ,  $\{DV_C\}_{SB}$  and  $\{DV_C\}_{WB}$  respectively) and interstitials are plotted together.

curve IV under high pressure, which means that the corresponding defects exhibit similar concentration distributions. In the high temperature and low pressure zone, the concentration maximum of  $\{FP_C-[100]_2\}_{WB}$  defect is much smaller than those of other defects, whose concentration maxima increase following the order of  $\{FP_C-[111]_4\}_{WB}$ ,  $\{FP_C-[111]_4\}_{SB}$ ,  $\{FP_C-[101]_3\}_{WB}$  and  $\{FP_C-[111]_3\}_{SB}$ . In the high temperature and high pressure zone, the maximum concentrations of  $\{FP_C-[111]_4\}_{WB}$ ,  $\{FP_C-[111]_4\}_{SB}$ , and  $\{FP_C-[111]_3\}_{SB}$  are the same order of magnitude.

Even if the lower bound is  $10^{-20}$ , the concentrations for all Zr-related defects are just higher than this lower bound at high temperatures of 1500 K or even 2600 K, see Fig. 14(a)–(e). This indicates that they are more difficult to detect. The concentration distribution of  $V_{Zr}$ ,  $\{SP\}_{SB}$  and  $\{SP\}_{WB}$  defects only locate at a narrow temperature and pressure range, especially true for  $\{SP\}_{WB}$ . While the concentration distribution zone of  $Zr_C$  defects is much wide, see Fig. 14(f). Except for  $Zr_C$  antisite defects, the concentration maxima of other defects appear in the low-pressure zone. According to the Arrhenius relationship, all concentration maxima of these defects do not exceed  $10^{-10}$ . At low pressures, the defect concentration maxima decrease in the order of  $I_{Zr}$ ,  $V_{Zr}$ ,  $Zr_C$ ,  $\{SP\}_{SB}$  and  $\{SP\}_{WB}$ , among which the concentration of  $\{SP\}_{WB}$  is much lower

than others. In the high-pressure zone, the concentration maximum of  $Zr_C$  is close to  $10^{-11}$  because of that the compressibility of the Zr-Zr bonds between the substituted Zr atom and the surrounding Zr atoms are much better than the original Zr-C bonds. It can be inferred from that the bulk modulus of Zr metal is smaller than that of ZrC.

Unlike  $V_{Zr}$ ,  $\{SP\}_{SB}$ , and  $\{SP\}_{WB}$  defects containing Zr vacancies, the concentration distribution of  $I_{Zr}$  defects runs through the entire pressure range, with a concentration maximum close to  $10^{-10}$  in low pressure zone, but with extremely low concentrations at high pressures. This phenomenon can be explained as follows. Under low pressure, the temperature rises and the lattice expands, Zr atoms are more likely to enter the interstitial sites of the lattice. But as the pressure increases, restricted by the large atomic radius of the Zr atoms, entering the interstitial sites becomes more difficult. The curves I and IV in Fig. 14(f) almost overlap, but the Gibbs energies of formation for the corresponding defects do not decrease monotonously with increasing temperature like the C interstitials and C Frenkel pairs, leaving quite different concentration distributions of  $V_{Zr}$  and  $\{SP\}_{SB}$ .

To facilitate the comparison of the concentration of the various defects discussed above, we have summarized their maxima at 0 GPa and 400 GPa in Table 5. In the high temperature and low pressure zone, the

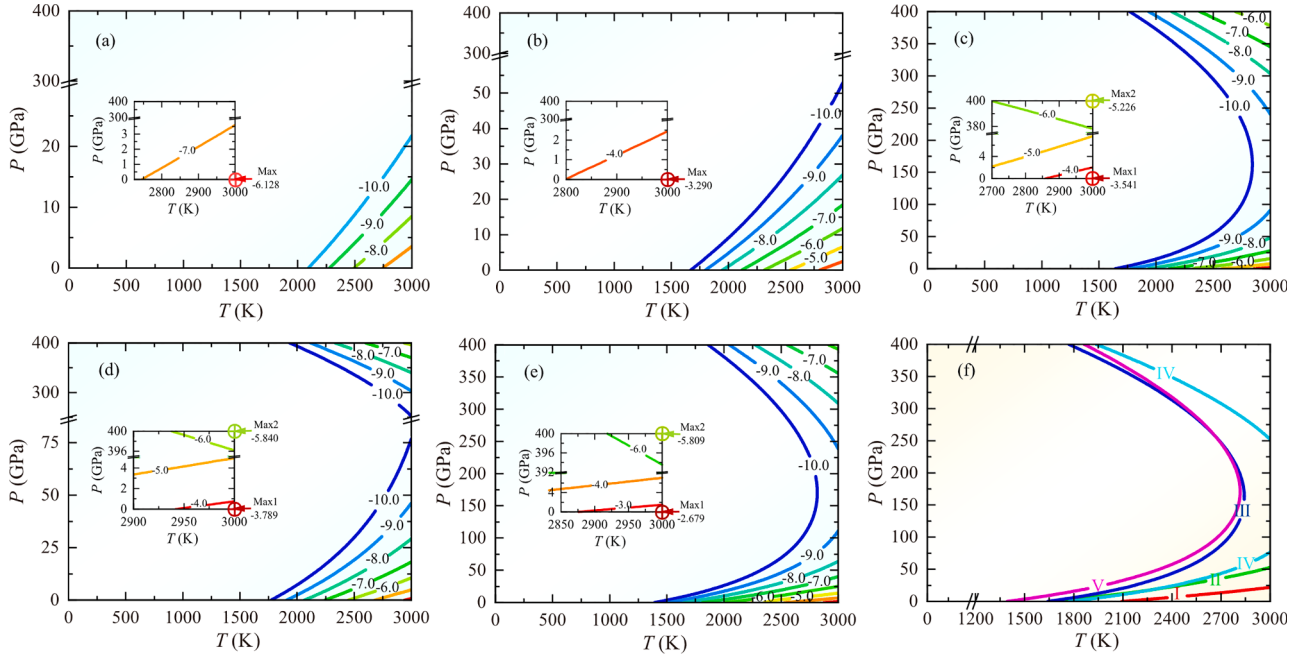


**Fig. 13.** Concentration distribution (log scale) of carbon Frankel defect pairs over a wide temperature and pressure range. The arrangement of the sub-pictures (a)–(f) is the same as the picture above but (a)–(e) and curves I–V in (f) correspond to  $\{\text{FP}_C\text{[100]}_2\}_{\text{WB}}$ ,  $\{\text{FP}_C\text{[101]}_3\}_{\text{WB}}$ ,  $\{\text{FP}_C\text{[111]}_4\}_{\text{SB}}$ ,  $\{\text{FP}_C\text{[111]}_4\}_{\text{WB}}$ , and  $\{\text{FP}_C\text{[111]}_3\}_{\text{SB}}$  respectively.

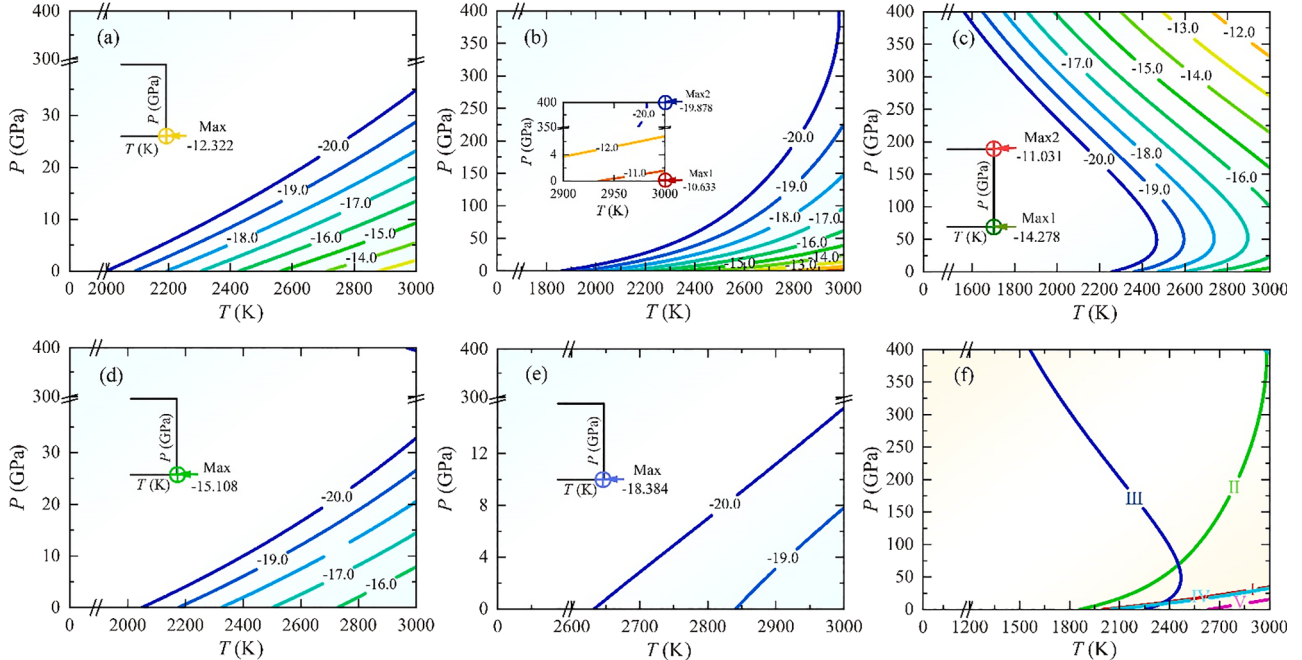


**Fig. 14.** Concentration distribution (log scale) of five types of Zr-related defects over a wide temperature and pressure range. (a)–(e) and curves I–V in (f) correspond to  $\text{V}_{\text{Zr}}$ ,  $\text{I}_{\text{Zr}}$ ,  $\text{Zr}_C$ ,  $\{\text{SP}\}_{\text{SB}}$ ,  $\{\text{SP}\}_{\text{WB}}$  respectively.

quasi-isolated C vacancies, the main defect in the crystal, will reach the highest concentration (up to 4.5%). The concentration of Zr vacancies is much lower than that of C vacancies, let alone Schottky pairs ( $\{\text{SP}\}_{\text{SB}}$  and  $\{\text{SP}\}_{\text{WB}}$ ). This result indicates that the probabilities of generating quasi-isolated Zr vacancies or Zr vacancies at the near neighbors of C vacancies are pretty low. In the high temperature and low pressure zone, linear carbon trimer (as shown in Fig. 4(b)) is the most favorable defect configuration (about 0.6%) except for C vacancies, an order of magnitude higher than the sum of the concentration of other C interstitial

defects (about 0.05%). Combining with the above discussion on the structures of Frenkel pairs, the existence of carbon vacancies neighboring maintains the angular carbon trimer stable, leaving  $\{\text{FP}_C\text{[111]}_3\}_{\text{SB}}$  with a very considerable concentration distribution (up to 0.2%) exceeding the sum of the concentration of several other types of Frenkel pairs (about 0.1%). From the comparison of the Gibbs energies of formation and concentrations of  $\{\text{DV}_C\}_{\text{SB}}$ ,  $\{\text{DV}_C\}_{\text{WB}}$ ,  $\{\text{SP}\}_{\text{SB}}$ ,  $\{\text{SP}\}_{\text{WB}}$ ,  $\{\text{FP}_C\text{[111]}_4\}_{\text{SB}}$  and  $\{\text{FP}_C\text{[111]}_4\}_{\text{WB}}$ , it seems that carbon vacancies prefer being the nearest neighbors and it's true for carbon vacancies

**Table 5**

Concentration maximum of various defects at 0 GPa or 400 GPa.

Defect type	$\log_{10} X$	
	0 GPa	400 GPa
V <sub>C</sub>	-1.347	-5.162
V <sub>Zr</sub>	-12.322	N
I <sub>C</sub> [1 0 0] <sub>2</sub>	-4.381	-13.984
I <sub>C</sub> [1 0 1] <sub>3</sub>	-2.223	-4.839
I <sub>C</sub> [1 1 1] <sub>5</sub>	-6.678	-2.028
I <sub>C</sub> [1 1 1] <sub>4</sub>	-3.349	-1.020
I <sub>Zr</sub>	-10.633	-19.878
Zr <sub>C</sub>	-14.278	-11.031
{DV <sub>C</sub> } <sub>SB</sub>	-2.950	-9.234
{DV <sub>C</sub> } <sub>WB</sub>	-3.552	-10.090
{SP} <sub>SB</sub>	-15.108	N
{SP} <sub>WB</sub>	-18.384	N
{FP <sub>C</sub> [1 0 0] <sub>2</sub> } <sub>WB</sub>	-6.128	-18.709
{FP <sub>C</sub> [1 0 1] <sub>3</sub> } <sub>WB</sub>	-3.290	-10.162
{FP <sub>C</sub> [1 1 1] <sub>4</sub> } <sub>SB</sub>	-3.541	-5.226
{FP <sub>C</sub> [1 1 1] <sub>4</sub> } <sub>WB</sub>	-3.789	-5.840
{FP <sub>C</sub> [1 1 1] <sub>3</sub> } <sub>SB</sub>	-2.679	-5.809

Note: The concentration data exceeding the lower bound  $10^{-20}$  are replaced with the letter "N".

with Zr vacancies or carbon interstitials.

At high temperature and high pressure, the concentration of carbon vacancies in ZrC crystals is greatly reduced. The isolated Zr vacancies will no longer be generated. Consequently, there will be no Schottky pairs assembled by Zr vacancies and C vacancies. The C interstitial defects I<sub>C</sub>[1 1 1]<sub>4</sub> and I<sub>C</sub>[1 1 1]<sub>5</sub> located in or near the tetrahedral interstitial site replace C vacancies and linear carbon trimers as the dominant defects (the total concentration of carbon trimers and carbon pentamers exceeds 10%). The concentration of carbon Frenkel pair with the similar interstitial configuration discussed above is still considerable. This means that high temperature and high pressure serve as advantages for the generation of C interstitial atoms located near the tetrahedral interstitial sites, and maintain a certain degree of aggregation with the C vacancies. Compared with other carbon interstitial defects, I<sub>C</sub>[1 0 0]<sub>2</sub> defect has fairly high Gibbs energy of formation and very low concentration, and the same is true for {FP<sub>C</sub>[1 0 0]<sub>2</sub>}<sub>WB</sub> compared with other Frenkel pairs due to the identical C dimer. Another notable thing is that the concentration of Zr<sub>C</sub> antisite defect is significantly higher than that at high temperature and low pressure and close to the lower bound set for carbon vacancies, interstitials and Frenkel pairs.

### 3.2.6. Defect interactions

To further clarify the relative distribution of key defects in ZrC and the effects of temperature and pressure, the characteristic interactions were explored. The interaction energies  $E_{\text{Inter}}$  between defects in ZrC can be obtained from the total energies of the supercells that contain a defect complex and the supercells with a single point defect. The interaction energies between two carbon vacancies and for a C vacancy with a Zr vacancy (SP) or a C interstitial atom (FP<sub>C</sub>) are given in Eqs. (12)–(14).

$$E_{\text{Inter}}(V_C - V_C) = E(DV_C) + E_{\text{perf}} - 2E(V_C) \quad (12)$$

$$E_{\text{Inter}}(V_{Zr} - V_C) = E(SP) + E_{\text{perf}} - [E(V_{Zr}) + E(V_C)] \quad (13)$$

$$E_{\text{Inter}}(V_C - I_C) = E(FP_C) + E_{\text{perf}} - [E(V_C) + E(I_C)] \quad (14)$$

From far to near, the interaction energies between defects in ZrC do not increase or decrease monotonously and the interactions for different neighbors are usually accompanied by some notable features. From Fig. 15, it seems that the 2nd and 3rd nearest-neighbor pairs of C-C divacancy, the first nearest neighbor pair of the C-Frenkel pair and the Schottky pair are the most noteworthy. For the carbon divacancy, it agrees well with Razumovskiy *et al.* [15] that there should be a strong carbon vacancy ordering in ZrC for the existence of strong repulsive

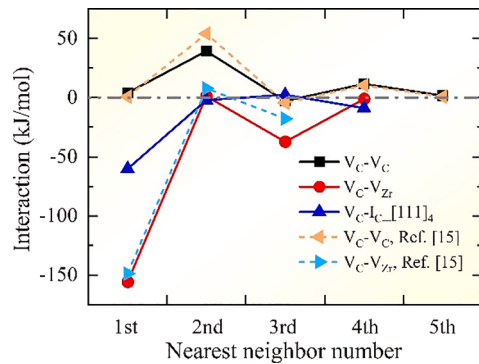


**Fig. 15.** V<sub>C</sub>-V<sub>C</sub>, V<sub>C</sub>-I<sub>C</sub>[1 1 1]<sub>4</sub> and V<sub>Zr</sub>-V<sub>C</sub> interactions in ZrC from the nearest neighbor to the furthest apart by *ab initio* calculations. The positive sign of interaction corresponds to repulsion between the defects, and negative to attraction.

interactions on the second coordination shell of C-C vacancy pair interactions. Furthermore, the size of the supercells we used to calculate the interactions is smaller, indicating that a higher concentration of carbon vacancies will be obtained, and results in a decrease of the repulsion between the two vacancies in the 2nd nearest-neighbor pair. The above situation can be reasonably described by the insight of Zhang *et al.* [59]. It was pointed out that when the concentration of carbon vacancies reaches a high level, the 2nd nearest-neighbor vacancy pairs will inevitably occur. For the Schottky pair, Razumovskiy *et al.* [60] inferred that the diffusion of metal atoms in ZrC is actually the migration of V<sub>Zr</sub>(V<sub>C</sub>)<sub>6</sub> vacancy clusters with C-Zr divacancy as the basic unit, which is attributed to the extremely strong attraction for the nearest neighbor C-Zr divacancy.

Combined with EOSs and the Debye model, we can obtain the Gibbs interaction free energy  $G_{\text{Inter}}$  including temperature and pressure effects. The interactions between two point defects from the strong bonding state to the weak bonding state are plotted as functions of pressure and temperature in Fig. 16. In some cases, the energy of the supercell containing a Schottky pair collapses seriously at ultrahigh pressure. And for the reasons that the concentrations of Schottky pairs reach the lower bound within a pressure of 35 GPa, we focus on the discussion for the interaction in the range of 0–100 GPa.

For carbon divacancies in Fig. 16(a), throughout the temperature and pressure range, the interaction energy for the second nearest neighbor carbon divacancy is always higher than that for other neighbor pairs, showing a strong repulsive effect. This indicates that even if the effects of temperature and pressure included, the carbon vacancies in ZrC are still in order. Besides, there is always an attraction between the two vacancies in the third nearest neighbor pair. The fingerprint configuration [59] at 0 K and 0 GPa is still energetically favorable at high temperature and pressure.

The interaction energy between the two vacancies in the first nearest neighbor pair decreases almost linearly with the enhancement of pressure, changing from a slight positive repulsion to a strong negative attraction. The interaction energies between vacancies in the 1st and 3rd nearest-neighbor pairs maintain a similar functional relationship with pressure at different temperatures compared to other neighbor pairs, which shows that the interactions between them seem to be less sensitive to temperature, that is, maintain high temperature stability. However, for other neighbor pairs in the range of 0–50 GPa or 300–400 GPa, especially in the former range, the interaction varies more drastically with temperature. At zero pressure, as the temperature increases, the interaction energies between vacancies in the 1st and 3rd nearest-neighbor pair have a slight increase and decrease respectively. Whereas other interaction energies increase significantly, with fluctuations reaching 50–75 kJ/mol per pair. In the pressure range of 0–50 GPa, at low temperature, the interaction energy between C vacancies

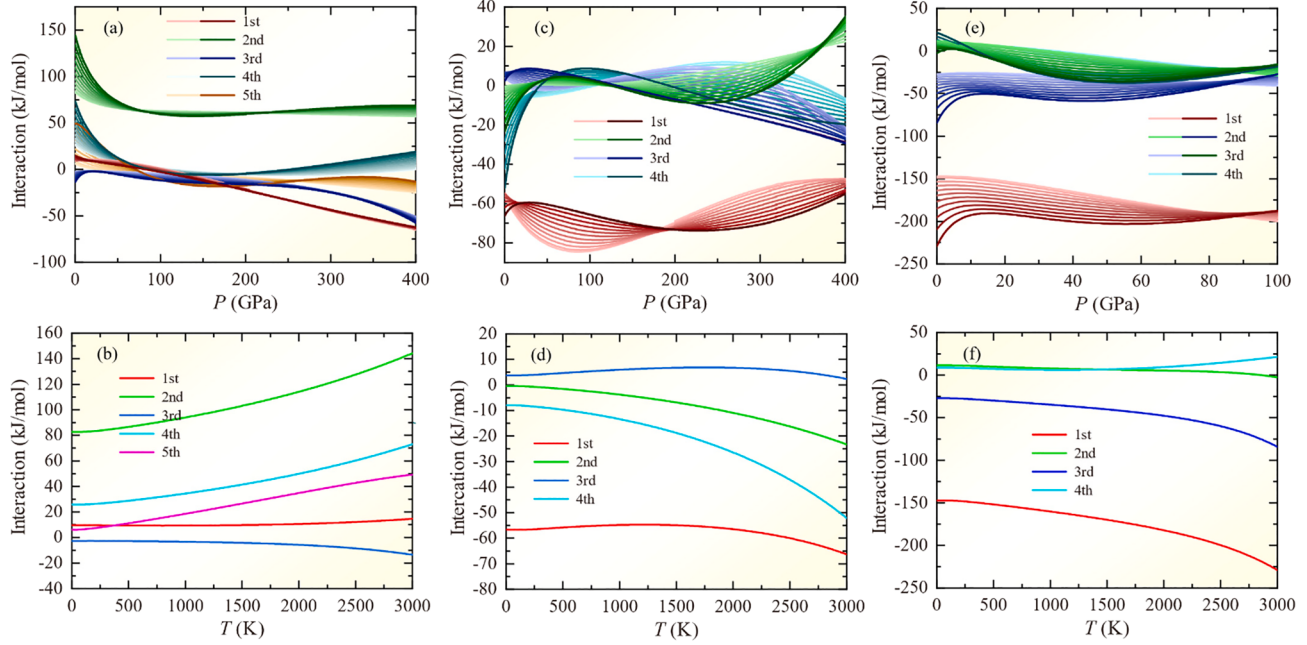


**Fig. 16.** Interaction energies between defects vary with pressure at different temperatures and vary with temperature at 0 GPa. (a)(b)  $V_C$ - $V_C$ , (c)(d)  $V_C$ - $I_C$ -[1 1 1]<sub>4</sub>, (e)(f)  $V_{Zr}$ - $V_C$ . In (a)(c)(e), the effect of temperature is indicated by gradient colors, and from low temperature to high, the line color changes from light to dark, with a gradient of 300 K.

increases in the order of  $G_{\text{Inter}}(3rd) < 0 < G_{\text{Inter}}(5th) \approx G_{\text{Inter}}(1st) < G_{\text{Inter}}(4th) \ll G_{\text{Inter}}(2nd)$ . At high temperature, it is in the order of  $G_{\text{Inter}}(3rd) < 0 < G_{\text{Inter}}(1st) \ll G_{\text{Inter}}(5th) < G_{\text{Inter}}(4th) \ll G_{\text{Inter}}(2nd)$ . Our result implies that high temperature is beneficial for the carbon vacancy ordering. When the pressure is further increased, in the range of 50–200 GPa, except for the second nearest neighbor carbon vacancy pair, the interaction energies between vacancies in other neighbor pairs are very similar. This result indicates that the probabilities of carbon vacancies appearing in these neighboring positions are the same to some extent. In the high pressure range of 250–400 GPa, the interaction energy is in the order of  $G_{\text{Inter}}(1st) < G_{\text{Inter}}(3rd) < 0 < G_{\text{Inter}}(5th) < G_{\text{Inter}}(4th) \ll G_{\text{Inter}}(2nd)$ .

The interaction energy between the carbon vacancy and the carbon interstitial atom in  $\text{PF}_C$ -[1 1 1]<sub>4</sub> affected by either temperature or pressure is much obvious and complicated than that between carbon vacancies. Compared with other nearest neighbor pairs, the interaction between the vacancy and interstitial for the 1st nearest neighbor carbon Frenkel pair can be kept to a minimum throughout the temperature and pressure range. The strongly bonded Frenkel pair is the most beneficial in terms of energy. At zero pressure, high temperatures reduce the interaction energies for all neighboring carbon Frenkel pairs.

Similarly, we divide the curves in Fig. 16(c) into several intervals. At 0–50 GPa and low temperature, except for the nearest neighbor pair, the interaction energy difference among several other neighbor pairs is very small, and the order of values is  $G_{\text{Inter}}(1st) \ll G_{\text{Inter}}(4th) < G_{\text{Inter}}(2nd) \approx G_{\text{Inter}}(3rd) \approx 0$ . However, as the temperature increases, the difference between the interaction energies gradually increases and the order is  $G_{\text{Inter}}(1st) < G_{\text{Inter}}(4th) < G_{\text{Inter}}(2nd) < 0 < G_{\text{Inter}}(3rd)$ . In the range of 50–200 GPa, from the second nearest neighbor pair to the fourth, the interaction energy difference among them is very small ( $\pm 10$  kJ/mol per pair). This result suggests that the probability that the carbon interstitial atom located in the non-nearest neighbor position is similar and much smaller. In the high pressure range of 250–400 GPa, as similar to the pair of carbon vacancies, the order is  $G_{\text{Inter}}(1st) < G_{\text{Inter}}(3rd) < G_{\text{Inter}}(4th) < 0 \ll G_{\text{Inter}}(2nd)$ .

Fig. 16(e) shows that in most cases the interactions between the C vacancy and Zr vacancy of Schottky pairs are attractive and the interaction energies of the 2nd and the 4th nearest-neighbor pairs are almost

the same. Similar to the  $\{\text{FP}_C$ -[1 1 1]<sub>4</sub> $\}_{\text{SB}}$ , the strongly bonded Schottky pair has an advantage from the energy point of view throughout the temperature and pressure range. At zero pressure, the temperature will slightly reduce, see Fig. 16(f), and elevate the interaction energies of the 2nd and the 4th nearest-neighbor pairs respectively. While for the 1st and the 3rd nearest-neighbor pairs, the interaction energies decrease significantly with the temperature, corresponding to the further increased attraction. In the range of 0–50 GPa and at low temperature, the interaction energies follow the order of  $G_{\text{Inter}}(1st) \ll G_{\text{Inter}}(3rd) < 0 < G_{\text{Inter}}(4th) \approx G_{\text{Inter}}(2nd)$ , while at high temperatures,  $G_{\text{Inter}}(4th) < G_{\text{Inter}}(2nd)$ . When the pressure increases, the order of the interaction energies is  $G_{\text{Inter}}(1st) \ll G_{\text{Inter}}(3rd) \approx G_{\text{Inter}}(2nd) \approx G_{\text{Inter}}(4th) < 0$ , indicating similar probabilities for non-nearest neighbor pairs.

#### 4. Conclusions

To clarify the existence and influence of defects in extreme service environments, we have studied the structural and physical properties in addition to the stabilities of various defects in ZrC by means of first-principles calculations. Within the framework of a quasi-harmonic Debye model, the thermophysical properties of ZrC with and without defects under varied pressure and temperature have been investigated and compared with available theoretical and experimental data. The calculated thermophysical quantities are consistent with available experimental and theoretical results. The introduction and aggregation of defects generally lead to a decrease in the bulk modulus and Debye temperature of ZrC, indicating that the performance of the material is in the face of the challenge of degradation. The same defect category, the similar degree of the influence.

The forming abilities and concentrations of various point defects in ZrC were evaluated and the defect distributions were examined. The dependences of the Gibbs energies of defect formation on temperature or pressure are closely related to the defect types. For defects with the same or similar configurations, their Gibbs formation energies and concentration distributions retain similar characteristics. For defect distributions, there are considerable concentrations of carbon vacancies, carbon interstitial atoms and carbon Frenkel pairs at high temperature and low pressure. Carbon vacancies are the main kind of defects. At high

temperature and high pressure, ZrC can accommodate a high concentration of carbon interstitial atoms near the tetrahedral interstitial site while the concentrations of other defects are significantly lower than that at low pressure. The Gibbs energies of formation and concentrations of point defects are sensitive to pressure in the lower pressure range. Therefore, applying a pressure is an effective way to inhibit the formation of large amounts of defects in ZrC.

The interactions between key point defects in neighboring positions were discussed. It was found that the defects in ZrC still have pronounced ordering characteristics including the effects of temperature and pressure. The prominent repulsion between C vacancies in the second nearest neighbor and the attraction in the third nearest neighbor are retained. The nearest neighbor positions in the Frenkel pair and Schottky pair always have advantages from the energy point of view. High temperature enhances the orderliness of defects. The orderliness has a process of firstly weakening and then strengthening as the pressure increases. When very high pressure is applied, the nearest neighbor defect pair is the most stable.

By clarifying the formation and distribution of the defects influenced by pressure and temperature, it is instructive to tailor the relevant properties of materials. Our first-principles insights might be useful in material design and defect engineering of ZrC-based materials and structures.

#### CRediT authorship contribution statement

**Guanlin Yang:** Conceptualization, Investigation, Data curation, Formal analysis, Writing - original draft. **Meiling Xiong:** Investigation, Formal analysis. **Yulu Zhou:** Supervision, Writing - review & editing, Funding acquisition. **Xiaoma Tao:** Supervision, Writing - review & editing, Funding acquisition. **Qing Peng:** Supervision, Writing - review & editing. **Yifang Ouyang:** Supervision, Writing - review & editing, Funding acquisition.

#### Declaration of Competing Interest

The authors declare that they have no known competing financial interests or personal relationships that could have appeared to influence the work reported in this paper.

#### Acknowledgements

All calculations were performed in the high-performance computing platform of Guangxi University. This work was financially supported by the National Natural Science Foundation of China (project Nos. 11964003 and 11865004) and the Guangxi Natural Science Foundation (project No. 2019GXNSFAA185058). Q. P. would like to acknowledge the support provided by the Deanship of Scientific Research (DSR) at King Fahd University of Petroleum & Minerals (KFUPM) through project No. DF201020.

#### References

- [1] E. Sánchez-González, O. Borrero-López, F. Guiberteau, A.L. Ortiz, Microstructural effects on the sliding-wear resistance of ZrC-MoS<sub>2</sub> triboceramics fabricated by spark-plasma sintering, *J. Eur. Ceram. Soc.* 36 (13) (2016) 3091–3097.
- [2] A. Rezapour, Z. Balak, Fracture toughness and hardness investigation in ZrB<sub>2</sub>-SiC-ZrC composite, *Mater. Chem. Phys.* 241 (2020), 122284.
- [3] Y. Xu, W. Sun, X. Xiong, Z. Zhan, T. Tian, Y. Chen, Z. Peng, Microstructure and ablation resistance of ZrC<sub>x</sub>N<sub>y</sub>-modified ZrC-SiC composite coating for carbon/carbon composites, *J. Eur. Ceram. Soc.* 38 (13) (2018) 4363–4372.
- [4] Y. Katoh, G. Vasudevanurthy, T. Nozawa, L.L. Snead, Properties of zirconium carbide for nuclear fuel applications, *J. Nucl. Mater.* 441 (1–3) (2013) 718–742.
- [5] A. Srivastava, B.D. Diwan, Elastic and thermodynamic properties of divalent transition metal carbides MC (M = Ti, Zr, Hf, V, Nb, Ta), *Can. J. Phys.* 90 (4) (2012) 331–338.
- [6] Z. Lv, H. Hu, C. Wu, S. Cui, G. Zhang, W. Feng, First-principles study of structural stability, electronic and elastic properties of ZrC compounds, *Phys. B* 406 (14) (2011) 2750–2754.
- [7] N. Rathod, S.K. Gupta, P.K. Jha, Dynamical stability and phase transition of ZrC under pressure, *Phase Transitions* 85 (12) (2012) 1060–1069.
- [8] M. Chauhan, D.C. Gupta, Electronic, mechanical, phase transition and thermophysical properties of TiC, ZrC and HfC: High pressure computational study, *Diam. Relat. Mater.* 40 (2013) 96–106.
- [9] A. Horvath, E. Rachlew, Nuclear power in the 21st century: Challenges and possibilities, *Ambio* 45 (1) (2016) 38–49.
- [10] Z.L. Chen, B. Li, G.H. Chai, Consideration of the maximum fuel temperature in safety review of HTR-PM, *Nucl. Saf.* 2 (2) (2012) 16–20.
- [11] J.u. Li, D. Liao, S. Yip, R. Najafabadi, L. Ecker, Force-based many-body interatomic potential for ZrC, *J. Appl. Phys.* 93 (11) (2003) 9072–9085.
- [12] S. Kim, I. Szlufarska, D. Morgan, *Ab initio* study of point defect structures and energetics in ZrC, *J. Appl. Phys.* 107 (5) (2010) 053521, <https://doi.org/10.1063/1.3309765>.
- [13] V.I. Razumovskiy, P.A. Korzhavyi, A.V. Ruban, *Ab initio* calculations of kinetic properties in ZrC and TiC carbides, *Solid State Phenom.* 172–174 (2011) 990–995.
- [14] Y. Zhang, J. Wang, B. Liu, J. Wang, H. Zhang, D.J. Green, Understanding the behavior of native point defects in ZrC by first-principles calculations, *J. Am. Ceram. Soc.* 97 (12) (2014) 4024–4030.
- [15] V.I. Razumovskiy, M.N. Popov, H. Ding, J. Odqvist, Formation and interaction of point defects in group IVB transition metal carbides and nitrides, *Comput. Mater. Sci.* 104 (2015) 147–154.
- [16] X. Yang, Y. Lu, P. Zhang, First-principles study of native point defects and diffusion behaviors of helium in zirconium carbide, *J. Nucl. Mater.* 465 (2015) 161–166.
- [17] M.-J. Zheng, I. Szlufarska, D. Morgan, Defect kinetics and resistance to amorphization in zirconium carbide, *J. Nucl. Mater.* 457 (2015) 343–351.
- [18] M. Jiang, J.W. Zheng, H.Y. Xiao, Z.J. Liu, X.T. Zu, A comparative study of the mechanical and thermal properties of defective ZrC, TiC and SiC, *Sci. Rep.* 7 (2017) 9344.
- [19] L. Chen, Q. Wang, L. Xiong, H. Gong, Mechanical properties and point defects of MC (M=Ti, Zr) from first-principles calculation, *J. Alloy. Compd.* 747 (2018) 972–977.
- [20] T.A. Mellan, A.I. Duff, M.W. Finnis, Spontaneous Frenkel pair formation in zirconium carbide, *Phys. Rev. B* 98 (17) (2018), 174116/1–12.
- [21] P.E. Blöchl, Projector augmented-wave method, *Phys. Rev. B* 50 (24) (1994) 17953–17979.
- [22] G. Kresse, J. Furthmüller, Efficient iterative schemes for *ab initio* total-energy calculations using a plane-wave basis set, *Phys. Rev. B* 54 (16) (1996) 11169–11186.
- [23] J.P. Perdew, K. Burke, M. Ernzerhof, Generalized gradient approximation made simple, *Phys. Rev. Lett.* 77 (18) (1996) 3865–3868.
- [24] M. Methfessel, A.T. Paxton, High-precision sampling for Brillouin-zone integration in metals, *Phys. Rev. B* 40 (6) (1989) 3616–3621.
- [25] A. Otero-de-la-Roza, V. Luana, Gibbs2: A new version of the quasi-harmonic model code. I. Robust treatment of the static data, *Comput. Phys. Commun.* 182 (8) (2011) 1708–1720.
- [26] M.A. Blanco, A.M. Pendás, E. Francisco, J.M. Recio, R. Franco, Thermodynamical properties of solids from microscopic theory: Applications to MgF<sub>2</sub> and Al<sub>2</sub>O<sub>3</sub>, *J. Mol. Struct. THEOCHEM* 368 (1996) 245–255.
- [27] M.A. Blanco, E. Francisco, V. Luana, GIBBS: Isothermal-isobaric thermodynamics of solids from energy curves using a quasi-harmonic Debye model, *Comput. Phys. Commun.* 158 (1) (2004) 57–72.
- [28] E. Francisco, J.M. Recio, M.A. Blanco, A.M. Pendás, A. Costales, Quantum-mechanical study of thermodynamic and bonding properties of MgF<sub>2</sub>, *J. Phys. Chem. A* 102 (9) (1998) 1595–1601.
- [29] T. Katsura, Y. Tange, A simple derivation of the Birch-Murnaghan equations of state (EOSs) and comparison with EOSs derived from other definitions of finite strain, *Minerals* 9 (12) (2019) 745.
- [30] H.L. Brown, C.P. Kemper, Elastic properties of zirconium carbide, *Phys. Status Solidi B* 18 (1) (1966) K21–K23.
- [31] D.J. Green (Ed.), *An Introduction to the Mechanical Properties of Ceramics*, Cambridge University Press, 1998.
- [32] C. Kral, W. Lengauer, D. Rafaja, P. Ettmayer, Critical review on the elastic properties of transition metal carbides, nitrides and carbonitrides, *J. Alloy. Compd.* 265 (1–2) (1998) 215–233.
- [33] A. Hao, T. Zhou, Y. Zhu, X. Zhang, R. Liu, First-principles investigations on electronic, elastic and thermodynamic properties of ZrC and ZrN under high pressure, *Mater. Chem. Phys.* 129 (1–2) (2011) 99–104.
- [34] C.P. Kemper, R.J. Fries, Crystallographic data. 189. Zirconium carbide, *Anal. Chem.* 32 (4) (1960) 570.
- [35] S. Mécabih, N. Amrane, Z. Nabi, B. Abbar, H. Aourag, Description of structural and electronic properties of TiC and ZrC by generalized gradient approximation, *Phys. A* 285 (3–4) (2000) 392–396.
- [36] A. Fernández Guillermet, Analysis of thermochemical properties and phase stability in the zirconium-carbon system, *J. Alloy. Compd.* 217 (1) (1995) 69–89.
- [37] A. Teresiak, H. Kubach, X-ray investigations of high energy ball milled transition metal carbides, *Nanostruct. Mater.* 6 (5–8) (1995) 671–674.
- [38] H.W. Hugosson, O. Eriksson, U. Jansson, B. Johansson, Phase stabilities and homogeneity ranges in 4d-transition-metal carbides: A theoretical study, *Phys. Rev. B* 63 (13) (2001), 134108/1–11.
- [39] A. Abdollahi, First-principle calculations of thermodynamic properties of ZrC and ZrN at high pressures and high temperatures, *Phys. B* 410 (2013) 57–62.
- [40] J. QIAN, C.-y. WU, H.-R. GONG, Phase transition, thermodynamic and elastic properties of ZrC, *Trans. Nonferrous Met. Soc. China* 28 (12) (2018) 2520–2527.
- [41] E.F. Westrum, G. Feick, Zirconium carbide: Heat capacity and thermodynamic properties from 5 to 350° K, *J. Chem. Eng. Data* 8 (2) (1963) 176–178.

- [42] W. Lengauer, S. Binder, K. Aigner, P. Ettmayer, A. Guillou, J. Debuigne, G. Grobott, Solid state properties of group IVb carbonitrides, *J. Alloy. Compd.* 217 (1) (1995) 137–147.
- [43] L.S. Levinson, High-temperature heat contents of TiC and ZrC, *J. Chem. Phys.* 42 (8) (1965) 2891–2892.
- [44] X.-G. Lu, M. Selleby, B.O. Sundman, Calculations of thermophysical properties of cubic carbides and nitrides using the Debye-Grüneisen model, *Acta Mater.* 55 (4) (2007) 1215–1226.
- [45] H. Fu, W. Peng, T. Gao, Structural and elastic properties of ZrC under high pressure, *Mater. Chem. Phys.* 115 (2-3) (2009) 789–794.
- [46] J. Zhu, B. Zhu, J.Y. Qu, Q.Q. Gou, F. Chen, Thermodynamic properties of cubic ZrC under high pressure from first-principles calculations, *Sci. China, Ser. G: Phys., Mech. Astron.* 52 (7) (2009) 1039–1042.
- [47] Y. Touloukian, R. Kirby, E. Taylor, T. Lee, Thermophysical properties of matter—the TPRC data series. Volume 13. Thermal expansion nonmetallic solids, IFI/Plenum, New York, 1977.
- [48] D. Varshney, S. Shriya, Elastic, mechanical and thermodynamic properties at high pressures and temperatures of transition metal monocarbides, *Int. J. Refract Metal Hard Mater.* 41 (2013) 375–401.
- [49] H. Li, L. Zhang, Q. Zeng, K. Guan, K. Li, H. Ren, S. Liu, L. Cheng, Structural, elastic and electronic properties of transition metal carbides TMC (TM = Ti, Zr, Hf and Ta) from first-principles calculations, *Solid State Commun.* 151 (8) (2011) 602–606.
- [50] V.I. Ivashchenko, P.E.A. Turchi, V.I. Shevchenko, First-principles study of elastic and stability properties of ZrC-ZrN and ZrC-TiC alloys, *J. Phys.: Condens. Matter* 21 (39) (2009) 395503, <https://doi.org/10.1088/0953-8984/21/39/395503>.
- [51] Y.A. Chang, L.E. Toth, Y.S. Tyan, On the elastic and thermodynamic properties of transition metal carbides, *Metall. Trans. 2* (1) (1971) 315–320.
- [52] S.F. Pugh XCII, Relations between the elastic moduli and the plastic properties of polycrystalline pure metals, *Phil. Mag.* 45 (367) (1954) 823–843.
- [53] L.E. Toth, Transition metal carbides and nitrides, Academic Press, New York, 1971.
- [54] F.I. Ajami, R.K. MacCrone, Thermal expansion, Debye temperature and Gruneisen constant of carbides and nitrides, *J. Less-Common Met.* 38 (2-3) (1974) 101–110.
- [55] R. Chang, L.J. Graham, Low-temperature elastic properties of ZrC and TiC, *J. Appl. Phys.* 37 (10) (1966) 3778–3783.
- [56] B. Liu, J.M. Wang, F.Z. Li, L.C. Sun, J.Y. Wang, Y.C. Zhou, Investigation of native point defects and nonstoichiometry mechanisms of two yttrium silicates by first-principles calculations, *J. Am. Ceram. Soc.* 96 (10) (2013) 3304–3311.
- [57] A.I. Duff, T. Davey, D. Korbacher, A. Glensk, B. Grabowski, J. Neugebauer, M.W. Finnis, Improved method of calculating *ab initio* high-temperature thermodynamic properties with application to ZrC, *Phys. Rev. B* 91 (21) (2015) 214311/1–8.
- [58] A. Zywiertz, K. Karch, F. Bechstedt, Influence of polytypism on thermal properties of silicon carbide, *Phys. Rev. B* 54 (3) (1996) 1791–1798.
- [59] Y.H. Zhang, B. Liu, J.Y. Wang, Self-assembly of carbon vacancies in substoichiometric ZrC<sub>(1-x)</sub>, *Sci. Rep.* 5 (2015) 18098.
- [60] V.I. Razumovskiy, A.V. Ruban, J. Odqvist, P.A. Korzhavyi, Vacancy-cluster mechanism of metal-atom diffusion in substoichiometric carbides, *Phys. Rev. B* 87 (5) (2013) 054203/1–7.